AFRL-RV-PS-
TR-2017-0125

ENHANCED CONTACTS FOR INVERTED METAMORPHIC MULTI-JUNCTION SOLAR CELLS USING CARBON NANOTUBE METAL MATRIX COMPOSITES

Brian J. Landi and Nathanael Cox

Department of Chemical Engineering
Rochester Institute of Technology
160 Lomb Memorial Dr.
Rochester, NY 14604-5603

18 Jan 2018

Final Report

AIR FORCE RESEARCH LABORATORY
Space Vehicles Directorate
3550 Aberdeen Ave SE
AIR FORCE MATERIEL COMMAND
KIRTLAND AIR FORCE BASE, NM 87117-5776

DTIC COPY
NOTICE AND SIGNATURE PAGE

This report is the result of contracted fundamental research which is exempt from public affairs security and policy review in accordance with AFI 61-201, paragraph 2.3.5.1. This report is available to the general public, including foreign nationals. Copies may be obtained from the Defense Technical Information Center (DTIC) (http://www.dtic.mil).

AFRL-RV-PS-TR-2017-0125 HAS BEEN REVIEWED AND IS APPROVED FOR PUBLICATION IN ACCORDANCE WITH ASSIGNED DISTRIBUTION STATEMENT.

//SIGNED//
DAVID WILT
Program Manager

//SIGNED//
PAUL HAUSGEN, Ph.D.
Technical Advisor, Spacecraft Component Technology

//SIGNED//
JOHN BEAUCHEMIN
Chief Engineer, Spacecraft Technology Division
Space Vehicles Directorate

REPORT DOCUMENTATION PAGE

Form Approved
OMB No. 0704-0188

1. REPORT DATE *(DD-MM-YYYY)*	2. REPORT TYPE	3. DATES COVERED *(From - To)*
18-01-2018	Final Report	30 Sep 2014 – 29 Dec 2017

4. TITLE AND SUBTITLE

Enhanced Contacts for Inverted Metamorphic Multi-Junction Solar Cells Using Carbon Nanotube Metal Matrix Composites

5a. CONTRACT NUMBER
FA9453-14-1-0232

5b. GRANT NUMBER

5c. PROGRAM ELEMENT NUMBER
62601F

6. AUTHOR(S)

Brian J. Landi and Nathanael Cox

5d. PROJECT NUMBER
8809

5e. TASK NUMBER
PPM00019605

5f. WORK UNIT NUMBER
EF123537

7. PERFORMING ORGANIZATION NAME(S) AND ADDRESS(ES)

Department of Chemical Engineering
Rochester Institute of Technology
160 Lomb Memorial Dr.
Rochester, NY 14604-5603

8. PERFORMING ORGANIZATION REPORT NUMBER

9. SPONSORING / MONITORING AGENCY NAME(S) AND ADDRESS(ES)

Air Force Research Laboratory
Space Vehicles Directorate
3550 Aberdeen Ave SE
Kirtland AFB, NM 87117-5776

10. SPONSOR/MONITOR'S ACRONYM(S)
AFRL/RVSV

11. SPONSOR/MONITOR'S REPORT NUMBER(S)
AFRL-RV-PS-TR-2017-0125

12. DISTRIBUTION / AVAILABILITY STATEMENT
Approved for public release; distribution is unlimited.

13. SUPPLEMENTARY NOTES

14. ABSTRACT

Development of inverted metamorphic multi-junction (IMM) solar cell technology has raised deployment issues regarding structure fracture from stress induced by packaging, vibration during transport, and operation. The proposed program involves development of a technique for fabricating carbon nanotube (CNT) metal matrix composites (MMC) to replace traditional electrodes in IMM solar cells. The fabrication of the MMCs will utilize CNT materials (i.e. SWCNTs, MWCNTs, etc.) from varying synthetic techniques, including novel methods of CNT deposition and metal to achieve stable composites.

15. SUBJECT TERMS
inverted metamorphic multi-junction, solar cell, carbon nanotube, metal matrix composites, MMC, single wall carbon nanotubes, multi wall carbon nanotubes

16. SECURITY CLASSIFICATION OF:			17. LIMITATION OF ABSTRACT	18. NUMBER OF PAGES	19a. NAME OF RESPONSIBLE PERSON
a. REPORT	b. ABSTRACT	c. THIS PAGE			David Wilt
Unclassified	Unclassified	Unclassified	Unlimited	48	19b. TELEPHONE NUMBER

--- This Page Intentionally Left Blank ---

TABLE OF CONTENTS

LIST OF FIGURES

LIST OF TABLES

ACKNOWLEDGMENTS

This material is based on research sponsored by Air Force Research Laboratory under agreement number FA9453-14-1-0232. The U.S. Government is authorized to reproduce and distribute reprints for Governmental purposes notwithstanding any copyright notation thereon.

DISCLAIMER

The views and conclusions contained herein are those of the authors and should not be interpreted as necessarily representing the official policies or endorsements, either expressed or implied, of Air Force Research Laboratory or the U.S. Government.

This Page Intentionally Left Blank

1 SUMMARY

In order to address issues related to mechanical and vibrational stresses that are commonly experienced in mounting, launch, and deployment of spacecraft, metal matrix composite (MMC) electrodes were fabricated with carbon nanotube (CNTs) as reinforcement. The research plans were centered on first developing and selecting appropriate processes for fabricating CNT-MMCs based on characterization of their material properties, followed by optimizing MMC designs based on electrical testing under stress. Efforts in the program were also directed toward implementing the CNT-MMCs into solar cell device processing in a process compatible with standard clean room procedures.

Layered style MMCs in which CNTs are embedded between Ag layers were rigorously characterized in terms of microstructure, mechanical, and electrical performance under stress. SEM (Scanning Electron Microscopy) analysis of fractures and the grain structure were used to understand the effects of CNT layer thickness on the over-coated Ag, and to observe CNTs mechanically bridging gaps in Ag upon fracture, thus demonstrating the utility of these advanced materials. In the process, an innovative method was used to fabricate free-standing Ag-single wall carbon nanotube (SWCNT) MMC thin films and the resulting films were characterized to understand their response to applied tensile stress through traditional tensile testing. The results were used to understand the appropriate CNT layer thickness needed to achieve reinforcement, and demonstrated improvements in the mechanical properties (i.e. toughness, strain-to-failure) as compared to pure Ag electrodes. Improvements in mechanical properties of the MMCs occurred as the SWCNT layer thickness was increased to 20 nm, exhibiting a 2.5x increase in toughness as compared to pure Ag electrodes. Higher SWCNT loadings led to degradation in performance. SEM analysis and mechanical results suggest that the MMCs transition from a reinforced structure to discrete layers between 20 nm and 50 nm SWCNT layer thicknesses. The highest performing MMC with 20 nm SWCNT layer corresponds to ~0.7 vol. % SWCNTs in the composite. The SEM analysis shows evenly distributed SWCNTs protruding from the fracture edges, which would likely prevent catastrophic failure under less dramatic stresses. The free-standing film mechanical testing and grain structure analysis provided the important first step toward understanding the optimum SWCNT loading in the MMCs and provides a fundamental basis for which further studies can expand and develop additional improvements for advanced MMC electrodes.

Fabrication processes and electrical testing procedures were also developed for assessing the electrical performance of CNT-MMC grid finger structures under stress. The grid finger structures utilized SWCNTs, multi-walled carbon nanotube (MWCNTs), or combinations thereof, and the processing techniques were all compatible with standard microelectronic engineering processes. The results of electrical testing and SEM analysis of the MMCs under stress suggest that SWCNT-MMC electrodes give an advantage over pure Ag electrodes. The SWCNTs are limited in crack-bridging capabilities, but are able to maintain electrical performance up to ~6 μm gap widths due to SWCNT length. Incorporation of much longer MWCNTs into the SWCNT-MMCs results in ~4× to 5× increase in crack-bridging capabilities, which may be useful if it is found that some solar cell or flexible electronics applications suffer from gaps larger than 6 μm. Additionally, assessment of an alternative to the large-diameter chemical vapor deposition (CVD) MWCNTs used in the initial hybrid RACK electrical tests

resulted in the selection of MWCNT materials from Nanocomp Technologies, Inc., which had small diameters, low defect content, and responded positively to traditional chemical and thermal purification techniques.

Finally, the CNT MMC fabrication process developed by RIT (Rochester Institute of Technology) was applied to commercial space solar cells, with demonstrations of both MWCNT and SWCNT MMC electrodes as top contacts. The as-fabricated cells all suffered from electrical shorting (between top and bottom cells) that was easily addressable by gently cleaning the edges with sandpaper, an issue that would not arise in standard production as the cells are not cleaved until after the top metallization is complete. Cells performed relatively well, operating at ~90% of the J_{sc} specification and just below the V_{oc} specification. The SWCNT MMC performed the best, reaching an efficiency of ~22%, compared to the typical ~29% factory specification. It is likely that the performance can be greatly improved by refining the lithography and other fabrication processes. This first attempt/success at integrating a fully clean room-compatible CNT-MMC fabrication process into state of the art triple junction space solar cells represents a very important step toward future adoption of the technology as a more robust electrode material. The implications extend beyond IMM devices to other solar markets, flexible electronics, and any other technology that may require more robust electrode materials.

2 INTRODUCTION

Enhancing the strength, ductility, and other mechanical properties of metal thin films would be beneficial to a variety solar energy markets. For instance, micro-cracks have been shown to cause decreased power output in single- and multi-crystalline Si PV modules [1-3]. Triple junction solar cells (ZTJ) used in space applications have experienced fracture issues, with 10% of the cells on spacecraft arrays requiring replacement pre-launch[4]. Inverted Metamorphic Multi-junction (IMM) offer both higher efficiency and dramatically reduced mass[5] as compared to traditional III-V solar cells, with significant potential for both space[6] and terrestrial concentrator[7] applications. These advanced solar cells, slated to replace triple-junction cells, are thinner and much more fragile, and will likely be even more susceptible to fracture damage. Cracks in solar cells cause loss of active cell area when a fracture propagates through the contact metallization, electrically disconnecting large portions of the cell. Thus, it is imperative that strategies be investigated to develop more robust metal electrodes.

A possible approach for attaining more robust electrodes is to replace the traditional thick silver conduction layer with a metal matrix composite (MMC) film that will have the needed combination of mechanical integrity (ductile matrix metal) and redundant electrical conduction paths to assure no loss in electrical connectivity due to cracks in the underlying solar cell. A MMC consisting of conductive fibers in a metal matrix can conduct electricity, even if the matrix is stressed to the point of fracture, provided the conductive fibers remain in electrical contact to both sides of the fracture. Carbon nanotubes (CNTs) are an attractive option for a reinforcement material as they are strong, flexible, conductive, and have been used as reinforcement in bulk metal matrix composites (MMCs) and coatings to increase yield strength[8], hardness[9, 10], and wear resistance[11, 12].

The objective of this research was to develop a fundamental understanding of carbon nanotube metal matrix composites (CNT-MMCs) as electrical contacts in IMM solar cells to alleviate issues caused by substrate stressing which can result in loss of solar cell performance. The proposed research plan was to develop processes for fabricating thin film CNT-MMC electrodes and to perform electrical/mechanical characterization of the CNT-MMCs, followed by optimization of design and fabrication parameters. The overarching goal was to demonstrate improved mechanical properties of the CNT-MMCs over traditional pure Ag and the ability of the CNTs to provide electrical connectivity when the Ag matrix is fractured, using a process that is fully compatible with standard semiconductor processing. A final demonstration of MMC fabrication and integration onto real triple junction solar cells was also proposed, given adequate time and funding. The following list summarizes the tasks proposed and pursued during this program, broken out by year. (It should be noted that Year 3 funding was not secured; however, RIT was able to make significant progress toward the first two tasks for year 3.)

Year 1: Develop fabrication process for CNT-MMC test structures and characterize metal grain structure, material properties, and electrical performance of the test structures.

- *Investigate different types of CNTs (Single wall, multi-walled, etc.) and CNT deposition techniques for MMC test structures.*

- *Evaluate surface uniformity, CNT morphology, and effects of CNT layer-thickness for the various CNT deposition techniques.*
- *Investigate metal deposition techniques (e.g. evaporation, sputtering, electroplating) onto CNT layers including characterization of metal grain structure, and establish procedures for varying grain structure and thin-film uniformity.*
- *Measure electrical resistance of CNT-MMC structures under stress and after fracture.*
- *Examine post-deposition techniques such as thermal annealing to improve electrical and mechanical properties of test structures.*
- *Initiate studies to develop processes for electrical isolation of MMC test structures.*

Year 2: Optimize parameters for selected CNT-MMC test structure designs and measure environmental stability towards IMM integration.

- *Investigate experimental parameters for depositing selected CNT type and metal technique from 1st year to optimize desired electrical performance and mechanical properties.*
- *Measure electrical resistance of optimized CNT-MMC structures under stress and after fracture.*
- *Characterize CNT-MMC test structures in relation to hardness and metal-CNT adhesion for optimized properties.*
- *Conduct relevant environmental testing of optimized MMC structures, such as thermal shock, thermal cycling, and ion irradiation conditions.*
- *Evaluate integration of MMC electrodes into the IMM device fabrication process and determine processes for electrical isolation of CNT-MMC structures.*

The sections that follow summarize the efforts regarding development of carbon nanotube metal matrix composite electrodes, including processing and fabrication, mechanical testing, and electrical testing under stress. These sections contain excerpts from publications which are references [32, 37-38].

3 METHODS, ASSUMPTIONS, AND PROCEDURES (MMC FABRICATION PROCESS DEVELOPMENT)

3.1 Introduction

The field of metal matrix composites (MMCs) has a long-standing history, yet the recent and continual development of new nanomaterials provides additional opportunities for its expansion. Carbon nanotubes have mechanical properties that make them an attractive option for reinforcement material, in terms of both tensile strength[13] and their high strain capabilities in response to applied stress[14]. The main challenges in fabricating CNT-MMCs are achieving homogeneous dispersions of CNTs in the metal matrix, high surface tension between most metals and CNTs resulting in low interfacial bond strength, and chemical/structural stability of the CNTs in metals processing. Much work regarding MMCs reinforced by CNTs has focused on developing bulk MMCs or thin-film coatings for wear resistance, but there has been little work done to assess the viability of thin film MMCs for use as a conducting electrode. There are a number of methods for fabricating MMCs, including powder metallurgy[8, 11, 15], thermal spraying[9, 16, 17], electrochemical deposition[18, 19], melting and sintering[20, 21] and physical vapor deposition for layer-style (sandwich) processing. Some of these methods (powder metallurgy, melting, and thermal spraying) are not practical from a solar cell processing perspective because of the high temperatures/pressures needed for fabrication, and additionally may be difficult to implement as a method to controllably deposit thin films with specific thickness requirements. It is still very difficult to make thin film MMCs in which CNTs are well dispersed. Consequently, the research conducted by Rochester Institute of Technology (RIT) utilized layer-style processing using PVD techniques (e-beam, thermal, sputtering) for metal deposition. Layered processing in which CNTs are embedded between deposited metal films is a technique that "few research groups have investigated", according to a review of carbon nanotube reinforced metal matrix composites[22]. Thus, the opportunity to develop CNT-MMC thin film fabrication techniques for IMM solar cells may provide experience and insights that extend to other applications as well, such as flexible electronics.

The effects of CNT layer thickness on the metal morphology and mechanical properties of CNT-MMCs are an important consideration for investigating techniques to fabricate layered thin film MMCs. In particular, the appropriate CNT film morphology and thickness needs to be identified to create composites which are truly reinforced and continuous, as opposed to composites that are simply discrete layers of metal and CNTs. Strategies for measuring the mechanical performance and properties of the CNT MMCs will also be necessary for demonstrating the utility IMM solar cells.

3.2 Initial MMC Experiments

The layered or "sandwich" style process, in which CNTs are embedded between evaporated Ag layers, was utilized for all MMC experiments. This process was chosen because of solar cell process compatibility, and because of the opportunities for development discussed in section 3.1. There are a number of CNT deposition techniques that could be useful in the layer-style processing, including thin-film transfer, ultrasonic spraying, and drop-casting. Additionally, different types of nanomaterials could be useful and may have select advantages as

reinforcement materials, including SWCNTs, MWCNTs, Ag nanowires, or even hybrids of these materials. For instance, SWCNTs have the most attractive electrical and mechanical properties, while MWCNTs are typicall longer and can be as little as one-one hundredth the cost of SWCNTs.

Initial experiments were conducted to attain proof-of-concept, showing that SWCNTs could be an effective crack-bridging reinforcement option. Thermal evaporation of Ti/Ag (5nm/250 nm) was performed on 175 µm thick semi-insulating (100) GaAs substrates through a shadow mask. The native oxide was removed by HCl (hydrochloric acid) immersion immediately before the deposition process. Following deposition, drop-casting of purified laser SWCNTs was performed onto the silver. The SWCNTs were dispersed in dimethylacetamide at a concentration of 0.6 µg/mL via bath sonication for 2 hours, and were then pipetted onto the GaAs substrates at 120 °C on a hotplate. Drop casting was followed by thermal oxidation in a muffle furnace at 300 °C for 2 hours to remove solvents and other residuals from processing. Another thermal evaporation of Ag (350 nm) was performed to topcoat the SWCNTs and create a Ti/Ag/SWCNT/Ag composite structure. The sample was mounted on carbon tape on an SEM sample stub and intentionally fractured with stainless steel tweezers. When observed by SEM following the fracture, images were acquired of both the Ag/SWCNT/Ag interface (Figure 1a), and gaps above the fracture lines (Figure 1b). The Ag/SWCNT/Ag interface clearly shows the edge of the fracture and that the SWCNTs have remained in the metal matrix despite the high stress of fracture. Additionally, images of the fracture revealed areas in which gaps as large as 3 µm long were bridged by SWCNTs. This represents an important step as proof that SWCNTs can physically bridge large gaps over a fractured substrate.

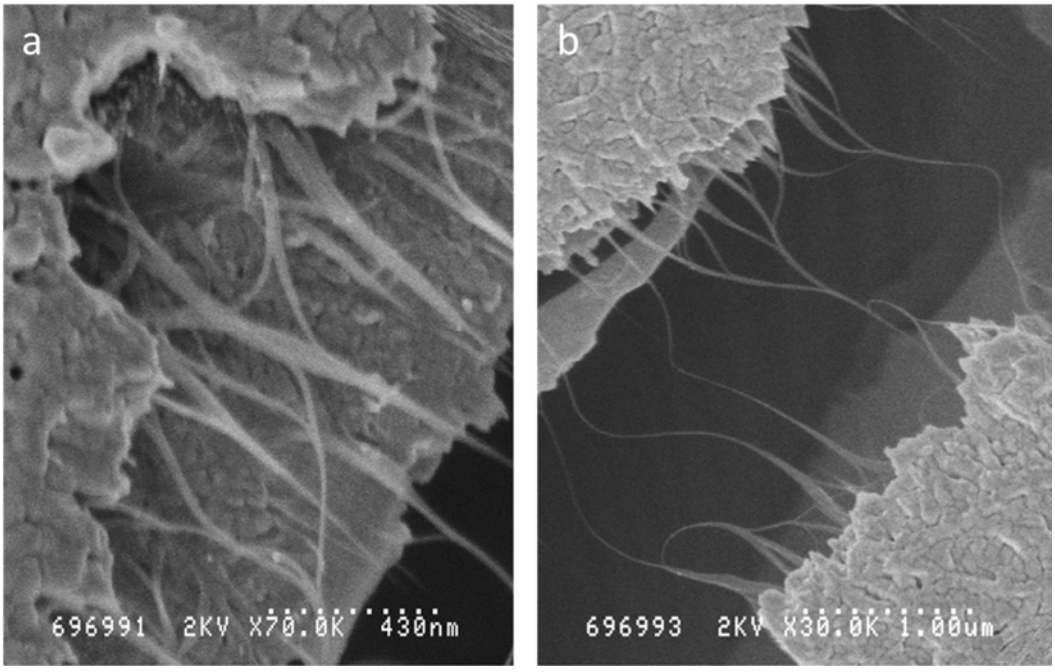

Figure 1. SEM images of (a) the interface of the 3 layers in the Ag/SWCNT matrix, and (b) SWCNTs bridging 3 µm gaps between the silver created by fracturing the substrate

3.3 CNT Deposition and Metal Microstructure Analysis

The drop-casting method described in the preliminary experiments demonstrated the crack bridging capabilities of SWCNTs, but there are inherent difficulties in the process that make this option less desirable. As the solvent evaporates the solution drops below the dispersion limit (~5 μg/mL) and the SWCNTs begin to re-bundle and will tend to agglomerate in certain areas. This is undesirable because for reliable SWCNT-metal composites the SWCNTs need to be uniformly distributed on the Ag base coat, in order to ensure that SWCNTs will be present to bridge any tensile cracks or fractures regardless of where they form. Thus, SWCNT thin film deposition by MCE transfer was utilized for further experiments to avoid agglomeration and provide a uniform CNT layer. Another benefit of the film deposition process, besides uniformity, is the fact that the thickness of the SWCNT film can be varied and easily controlled by controlling both the volume and concentration of the starting dispersion prior to filtration onto the MCE filters.

Experiments were conducted with SWCNT films of varying thickness to determine the appropriate SWCNT weight loading for creating robust MMC structures. Test structures were prepared by first depositing a Ti/Ag (6 nm/500 nm) base-layer on a GaAs wafer via thermal evaporation. Prior to the thermal evaporation the native oxide on the GaAs wafer was removed by soaking in HCl. SWCNT films were deposited onto the Ag base-layer by the standard MCE transfer process. The resulting sample was purified through thermal oxidation at 300°C in air for 2 hours. An additional 500 nm of silver was thermally evaporated over a portion of the SWCNT thin-film and Ag base-layer. The thickness of the SWCNT films was adjusted by varying the mass of the SWCNTs, creating films with different areal densities. For instance, an areal density of 10 $\mu g/cm^2$ corresponds to ~ 100 nm thick SWCNT film, as measured by profilometry. Initially, 10 $\mu g/cm^2$ and 30 $\mu g/cm^2$ SWCNT films were used to fabricate the MMCs. A cross-section of the MMC structures shown as the inset in Figure 2 allows for analysis of the Ag top-layer morphology in relation to both the SWCNT film (left of dash) and the underlying metal (right of dash). Scanning electron microscopy (SEM) analysis of the Ag top-layer over the 10 $\mu g/cm^2$ SWCNT film is shown in Figure 2a, wherein the observed Ag grain structure is small, with many discrete particles. The Ag grain structure over the 30 $\mu g/cm^2$ SWCNT produced nearly identical results. In contrast, Figure 2b shows the SEM results of the Ag top-layer deposited directly onto the Ag base-layer, which has much larger grain structure compared to the Ag deposited onto the SWCNTs. The observed difference in grain structure based on the underlying substrate suggests that there is little interaction between the Ag top-layer and the Ag base-layer over the SWCNT films. These observations motivate further understanding of the effect of the SWCNT film thickness on the final metal grain structure. It is unknown at this time whether a harder film (more grain boundaries) or a more ductile film (continuous) is desirable during a fracture event.

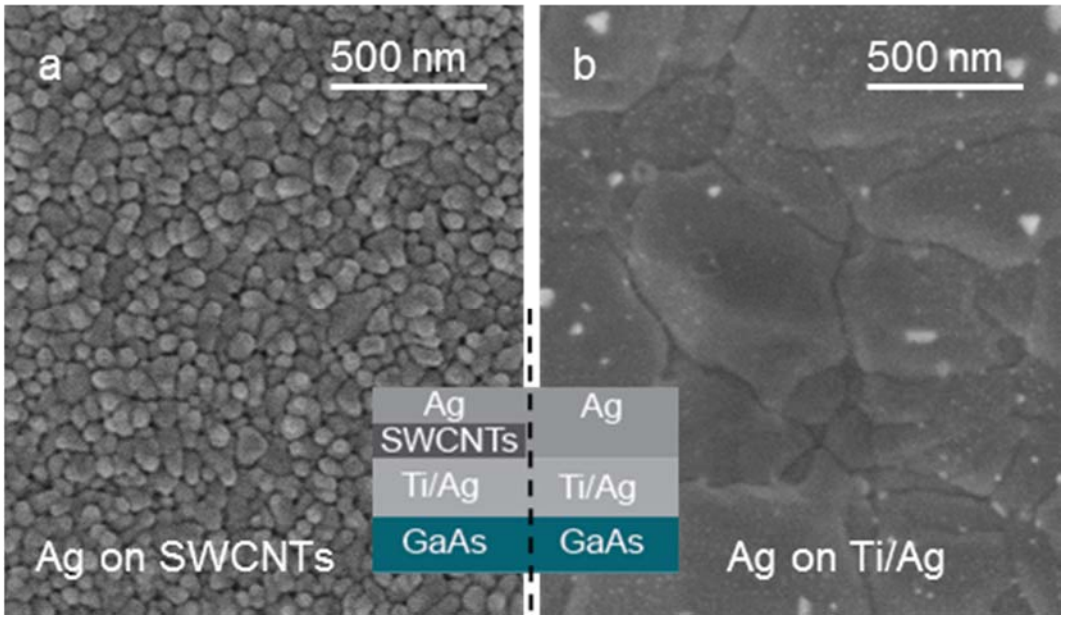

Figure 2. SEM images at 50,000× magnification show the Ag top-layer (a) over the SWCNT thin film (10 µg/cm2) and (b) over the Ti/Ag base-layer.

Note: The inset figure is a cross-section of the MMC

It is presumed that if the SWCNT film is sufficiently thick, then the Ag-SWCNT-Ag composite will exhibit discrete layers, and upon substrate fracture these discrete layers may delaminate due to stress at the film interfaces. Some delamination was observed at the SWCNT interface in the initial test structures for SWCNT film thicknesses of 30 µg/cm^2. It is thus imperative to determine the optimal areal density of SWCNTs necessary for *reinforcement*, rather than *discrete layers*. Reinforcement implies that the SWCNT network is sufficiently thin and porous to allow the Ag top-layer to penetrate through the SWCNT network and nucleate both on the SWCNTs and the Ag base-layer, thus forming a continuous structure. The concepts of reinforced and discrete layer regimes are illustrated graphically in Figure 3.

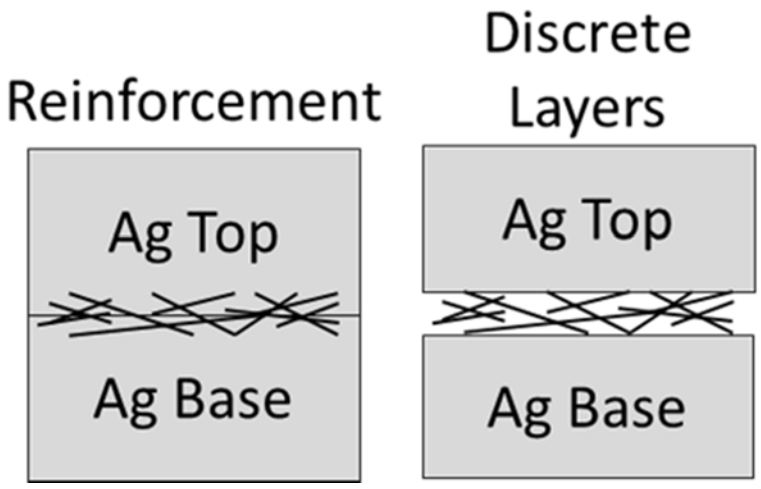

Figure 3. Conceptual rendering showing the difference between reinforcement and discrete layer regimes in sandwich-style CNT-metal matrix composite structures

Five SWCNT thin-films, with areal densities of 1 μg/cm^2, 2 μg/cm^2, 5 μg/cm^2, 10 μg/cm^2, and 30 μg/cm^2, were prepared and transferred onto the Ti/Ag base-layer using the standard MCE transfer method. The thicknesses of the corresponding thickness of the SWCNT films are approximately 10 nm, 20 nm, 50 nm, and 100 nm, as estimated based on profilometry measurements. SEM analysis was employed to gain a qualitative assessment of the thin-film morphology, silver grain structure, and MMC quality. The schematic in Figure 4 depicts the fabrication processing steps.

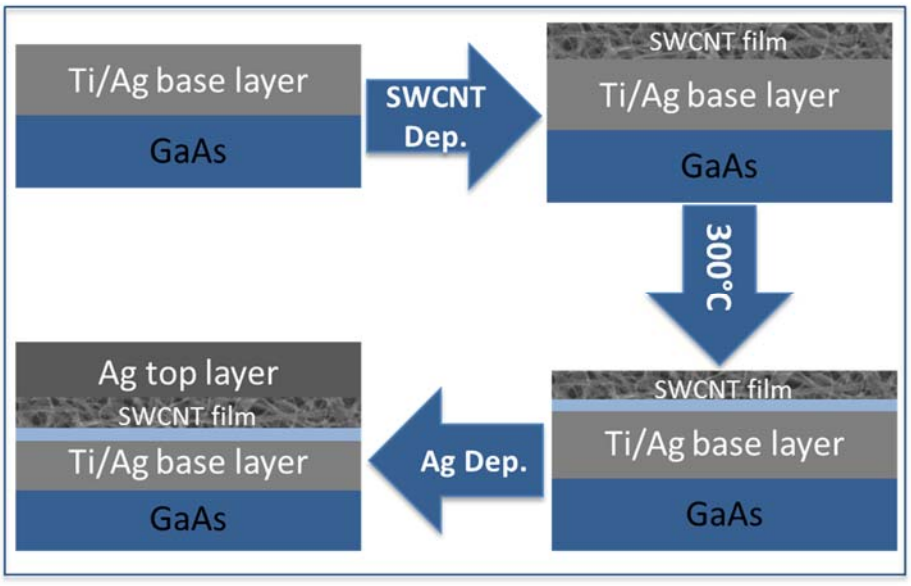

Figure 4. The schematic depicts samples processed with the Ti/Ag (10 nm/500 nm) base-layer thermally evaporated on GaAs.

Note: SWCNT thin-film deposition, thermal oxidation at 300°C for 2 hours, followed by thermal evaporation of the Ag (500 nm) top-layer

Figure 5 shows representative SEM micrographs corresponding to each SWCNT thin-film areal density used in the experiment. The larger grain size and reduced grain boundaries for the Ag deposited on 1 μg/cm^2, 2 μg/cm^2, and 5 μg/cm^2 SWCNTs (Figure 5 b, c, and d, respectively) is immediately apparent compared to the 10 μg/cm^2 and 30 μg/cm^2 sample (Figure 5 e and f). Qualitative analysis of the three samples with the lowest areal density consistently shows that the 1 μg/cm^2 sample exhibited the largest Ag grain size, closely resembling the grain structure of the Ag-only control samples; however, the 2 and 5 μg/cm^2 samples are very similar. It is evident from these differences in metal morphology that the SWCNT surface has an impact on the grain structure of the over-coated Ag. These qualitative observations of Ag grain structure can be quantified by particle size analysis in *ImageJ*.

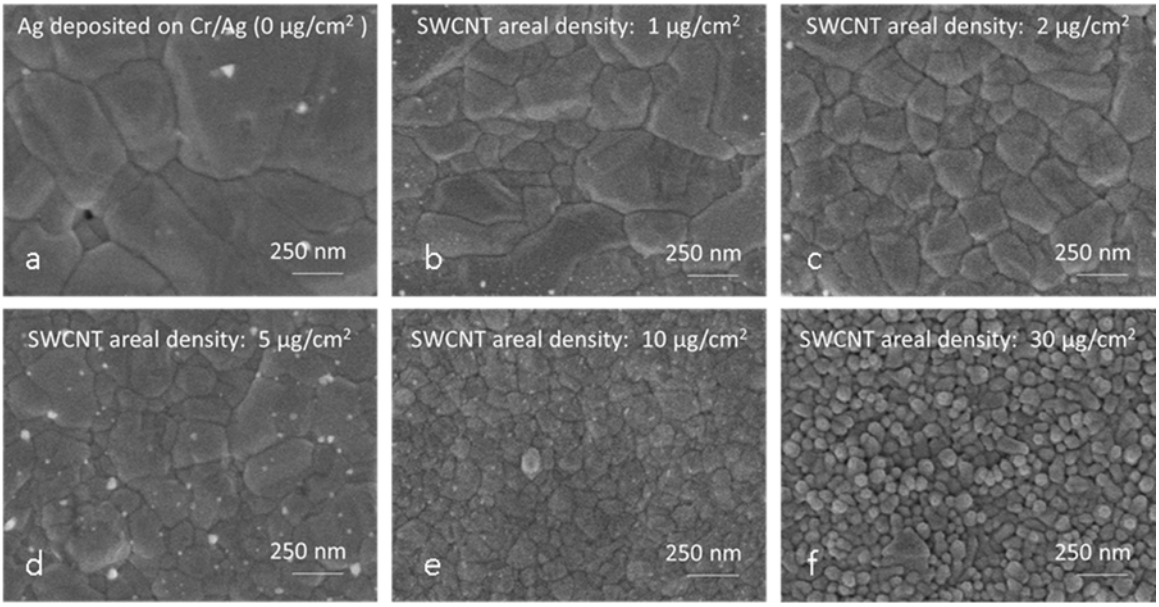

Figure 5. The SEM images at 50,000× magnification for the Ag grain structure of the 500 nm Ag top-layer deposited onto SWCNT thin-films with areal densities of (a) 0 μg/cm^2 (Ag control) (b) 1 μg/cm^2, (c) 2 μg/cm^2, (d) 5 μg/cm^2, (e) 10 μg/cm^2, and (f) 50 μg/cm^2

Analysis of the micrographs in Figure 5 was conducted using *imageJ*. The *fast Fourier transform bandpass filter* function was used to sharpen the images, and *thresholding* was applied between 70 and 255 digital counts to highlight the individual grains. The *particle analyzer* function was used to obtain grain size distributions. The grain size was determined by calculating the diameter of each Ag grain based on the measured area (assuming a circular geometry). The results are shown in Figure 6, and corroborate the qualitative observations concerning the Ag grain structure. Based on this analysis, it is proposed that the discrete layer regime occurs at SWCNT loadings ≥ 10 μg/cm^2. However, measurement of other material properties may be necessary to more accurately determine the crossover between *reinforcement* and *discrete layers*. It is not presently understood why the dramatic grain structure change between 5 and 10 μg/cm^2 occurs. One possibility is that the change is related to interactions of the Ag with the substrate, because of the similarities between the thinner samples. The grain structure is largest for the thinnest SWCNT sample, which implies the Ag may more effectively penetrate through the network to the base-layer, thus increasing the contributions of the base-layer to the overall grain

structure. As the thickness increases, the effect of the SWCNT morphology on the final grain structure also increases.

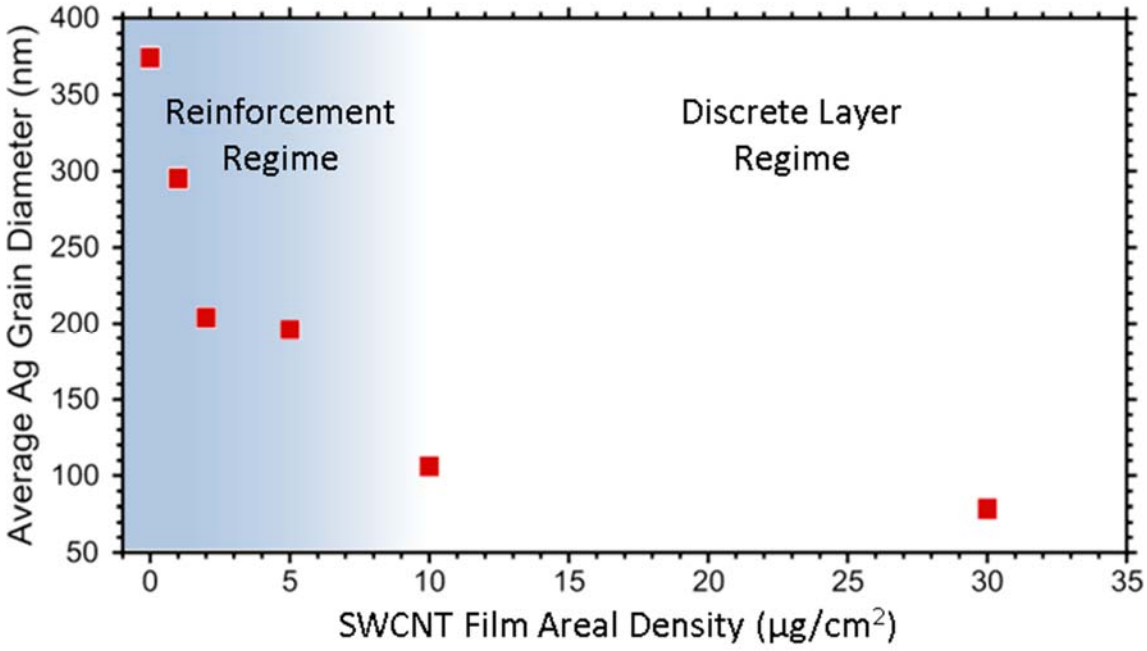

Figure 6. The results of image analysis of the Ag grain diameter as a function of SWCNT film areal density

4 MMC MECHANICAL CHARACTERIZATION

4.1 Introduction

In addition to correlating mechanical properties of MMCs to the grain structure analysis discussed in section 3.3, it is additionally important to demonstrate improvements in mechanical properties of the MMCs compared to traditional Ag electrodes. Investigation of the mechanical performance of thin film MMCs has been limited, due to difficulty in preparing and testing samples by conventional methods. Previous research dedicated to this topic often employs complex methodology for fabricating and/or testing free-standing thin films because of difficulties associated with handling and clamping the delicate samples for tensile tests [23-27]. Therefore, improved fabrication methods which enable measurement of traditional stress-strain relationships in metallic thin films can also aid in characterization of advanced MMC concepts.

The following sections describe a streamlined process for producing free-standing metallic films that enables traditional dynamic mechanical analysis. The process was also adapted to create layered thin film MMCs by embedding SWCNTs between two Ag layers, and the SWCNT weight loading has been systematically varied to improve mechanical properties of the MMCs as compared to Ag-only films.

4.2 Materials and Methods

Ag control samples and Ag-SWCNT MMCs were fabricated as free-standing films (FSFs) for tensile testing. Polyvinylchloride (PVC) tape was mounted onto a glass slide and laser-cut to create a dog-bone patterned mask (Figure 7a). Ag was deposited at a thickness of 1.5 μm over the PVC mask via thermal evaporation, and the mask was subsequently removed (Figure 7b). For the Ag control samples, an additional 1.5 μm Ag was deposited over the base-layer in a second deposition step. MMC samples were prepared by transferring high purity SWCNT films onto the Ag base-layer (using a previously described method [28]) and were subsequently over-coated with an additional 1.5 μm Ag. The SWCNTs used in this study were synthesized in-house by laser vaporization (Ni/Co catalyst, 1150 °C) in Argon atmosphere. The raw soot was purified via acid reflux (HCl, HNO_3) for 16 hours, followed by thermal oxidation (560 °C, with a ramp-stop at 10 °C/minute) [29]. The samples were additionally soaked in HCl to remove any additional catalyst particles and the thermal oxidation repeated to further remove amorphous carbon. The purity of the sample was determined to be equivalent to a 100% pure reference sample, as determined by ultraviolet (UV)-visible optical absorption spectroscopy [30]. The typical diameters of the purified SWCNTs as determined from the radial breathing modes (Raman spectroscopy analysis) [31] were between 1 nm and 1.4 nm. SWCNT thin films were prepared by dispersing SWCNTs in 2wt.% sodium dodecyl-sulfate (SDS) by horn sonication for 5 hours, followed by vacuum filtration onto a mixed cellulose ester (MCE) membrane. The resulting SWCNT films were transferred face-down onto the already deposited Ag dog-bone structure, and the MCE membrane was dissolved away by successive acetone baths.

Both the Ag control and MMCs were released from the substrate by partial liftoff of one end of the dog-bone structure from the glass with Kapton tape (Figure 7c). The tape was attached to a small Kapton film “anchor” (Figure 7d), which prevents the structure from curling up due to

stress and alleviates issues related to handling/clamping the films for tensile testing. These steps were repeated at the opposite end of the structure to fully release it from the glass slide, thus creating a FSF (Figure 7e). The dog-bone structures shown in Figure 7 consist of wide "paddles" on each end, a tapered region, and a narrow region. The total length of the structures is 2.8 cm long, with paddle dimensions of 5 mm x 5 mm. The tapered regions are 4 mm long with radius of curvature of 14.25 mm, and the narrow region had dimensions of 2 mm wide x 6 mm long.

The SWCNT loading in the MMCs was varied by depositing SWCNT films of varying areal densities, including 1, 2, and 5 μg/cm^2, corresponding to film thicknesses of ~10, 20, and 50 nm, respectively. Control of the areal density of the films was achieved by changing the volume of a fixed concentration (10 μg/mL) of SWCNT/SDS dispersion used when filtering the solution onto the MCE membrane. Film thickness was measured by contact profilometry using a Tencor P2 Profilometer.

The Ag grain structure of each FSF was characterized by scanning electron microscopy (SEM). The mechanical properties were quantified by tensile testing using a TA Instruments Q800 dynamic mechanical analyzer at room temperature, by clamping the Kapton anchors and pulling in opposite directions at a constant strain rate of 0.05 %/min until failure.

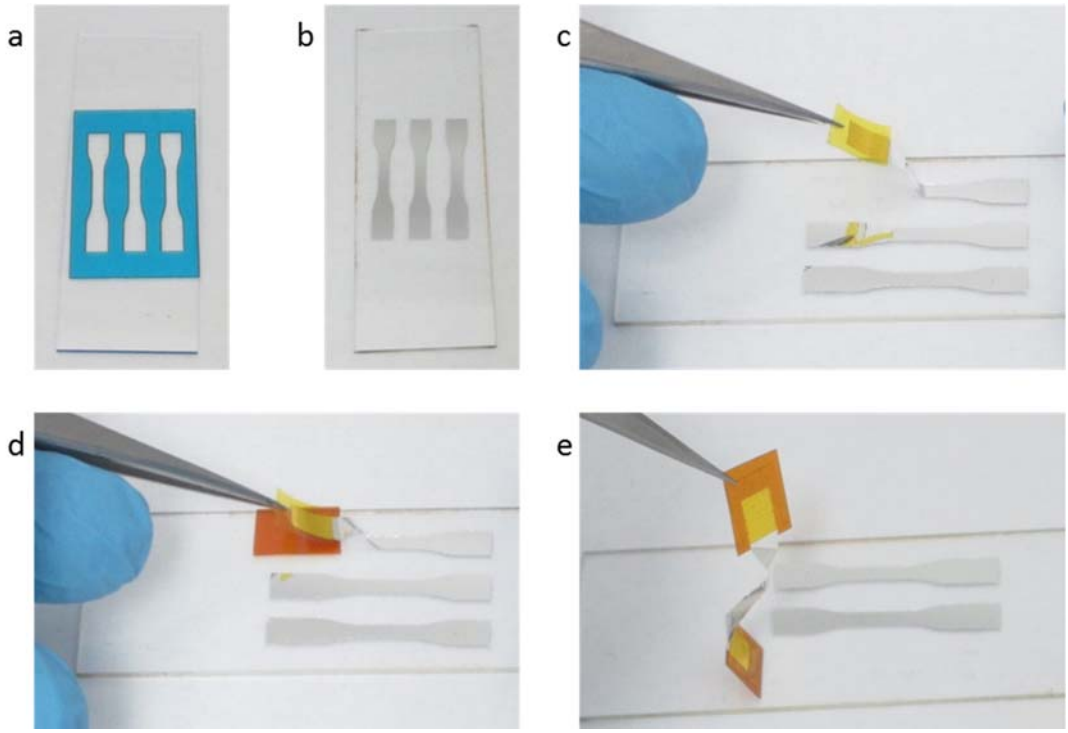

Figure 7. Photographs showing the fabrication steps for creating free-standing thin films: (a) Dog-bone structures laser-cut into PVC tape mounted on a glass slide, (b) thermally evaporated Ag and removal of the sacrificial PVC, (c) Kapton tape used to peel up one end of the structure, and (d) attached as "anchor", (e) free-standing film is fully released from the substrate by repeating steps c and d

4.3 Results and Discussion

Tensile testing of each Ag and MMC FSF was performed to assess potential benefits of incorporating SWCNTs into the Ag matrix in terms of strength and/or ductility. The representative stress-strain curves resulting from tensile testing of the constructed sample set of FSFs with increasing SWCNT loading are shown in Figure 8a. The results clearly show that the addition of SWCNTs to the Ag matrix changes the response to applied stress. Figure 8b shows the ultimate tensile strength (UTS) as a function of SWCNT layer thickness. The UTS increases from 243 MPa for the Ag control sample to a maximum value of 315 MPa for the MMC with 20 nm SWCNT film thickness, which is followed by a marked decrease in UTS for the highest SWCNT loading. Figure 8c shows the strain-to-failure as a function of SWCNT loading, which is similar to, yet more pronounced than the UTS trend. The strain-to-failure for Ag control is 1.1%, which increases by ~2x with a 20 nm SWCNT layer, and again decreases at a 50 nm SWCNT layer thickness. The UTS and strain-to-failure for the Ag control are comparable to similar Ag films described in other work, which were fabricated and measured by more complex techniques [27]. The improvements in UTS for the MMCs are attributed to the high intrinsic strength of individual SWCNTs which have been shown to be ≥ 20 GPa [13]. The improvement in strain-to-failure is likely due to a combination of elastic strain for individual SWCNTs (reported to be as high as 5.8% [14]) and some reorientation of the random SWCNT network under stress. For comparison, the SWCNT thicknesses of 10, 20, and 50 nm employed in the current study would result in relative SWCNT volume % values of ~0.3%, 0.7%, and 1.6%, respectively, if the thickness is assumed to be uniform and solid. In reality, the nanoscale porosity of SWCNT films will reduce the volume % by some portion depending on the processing and metal penetration depth into the film. However, the impact of the MMC testing shows that addition of low volume % SWCNTs can directly result in an enhancement in mechanical properties.

The collective improvements in mechanical properties are further expressed in terms of toughness, which incorporates aspects of both strength and strain. Toughness values are calculated as the integral of the stress-strain plots in Figure 8a, and are shown as a function of SWCNT loading in Figure 8d. The toughness increases from 1.66 MJ/m^3 for the Ag film to a maximum of 4.13 MJ/m^3 with incorporation of 20 nm SWCNT films, which is followed by a dramatic decrease in toughness for the MMC with 50 nm SWCNT layer thickness. Based on the measured increase in mechanical performance up to 20 nm SWCNTs, it is likely that the SWCNTs are providing reinforcement in the MMCs. Reinforcement is expected to occur when the top-layer of Ag penetrates through the SWCNTs to the Ag base-layer, creating a continuous structure. The structure with 50 nm SWCNT layer shows a reduction in mechanical properties compared to Ag in all cases, which suggests that the structure consists of discrete layers where the overall performance is dictated by the individual layers in response to an applied stress. Therefore, from a mechanical perspective, there is a clear benefit to utilizing SWCNTs as a reinforcement in MMC thin films, as evidenced by the 2x increase in strain-to-failure and ~2.5x overall increase in toughness. The results also suggest that the mechanical properties could be further improved with increased SWCNT loading by incorporating multiple thin SWCNT layers within the MMCs.

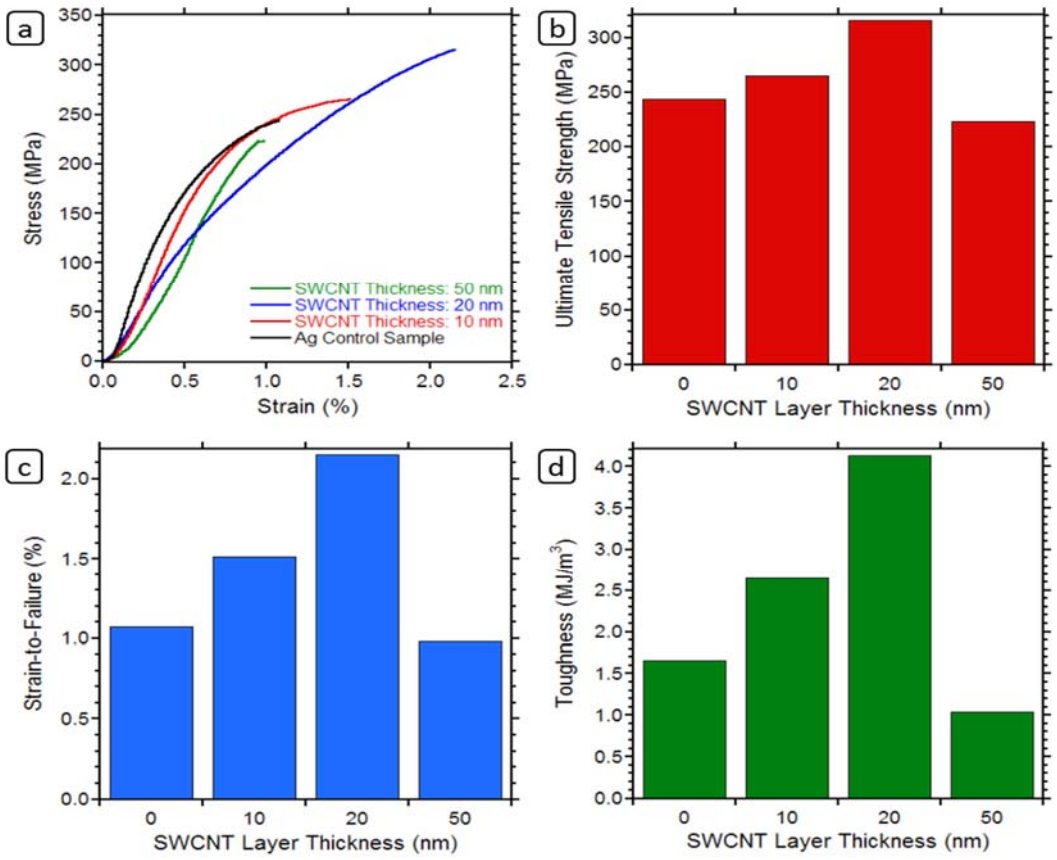

Figure 8. (a) Plots of stress versus strain for Ag control and MMC free-standing films with SWCNT layer thicknesses of 10, 20, and 50 nm and the properties of (b) ultimate tensile strength, (c) strain-to-failure, and (d) toughness are plotted as a function of SWCNT layer thickness

SEM analysis of each FSF was performed for an assessment of the Ag grain structure, and to ascertain the relationship between grain structure and mechanical performance. Figure 9a-d shows SEM micrographs of the Ag surface of the FSFs characterized in Figure 8. The trend in Ag grain size was quantified with a minimum of 550 measurements for each sample with ImageJ software to determine the Martin diameters of the Ag grains. The average grain diameter for the Ag control is measured to be ~177 nm. As the SWCNT film thickness increases, the average top Ag grain diameter systematically decreases to a value of ~95nm for an MMC with 50 nm SWCNT film. These measurements are consistent with the previous grain structure analysis discussed in section 3.3 with similar MMCs deposited on GaAs, wherein asymptotic behavior of the grain size was observed for SWCNT thicknesses greater than 50 nm [32]. The decrease in Ag grain diameter follows the expectation that high surface tension between Ag and SWCNTs affects grain growth, which is also supported by recent published claims which attributed decreased grain size to SWCNTs pinning metal grain boundaries [33].

The mechanical properties (e.g. yield strength, hardness, UTS, etc.) for metals are known to be proportional to the inverse square root of grain diameter by the Hall-Petch relationship [34, 35]. In the present case, it follows that the ultimate strength of the MMCs should increase with

increasing SWCNT loading, which has previously been reported for Ti-SWCNT bulk composites [33]. The mechanical data in Figure 8b initially shows Hall-Petch behavior, with an increase in strength as grain size decreases (and SWCNT thickness increases). However, the sharp decrease in strength for the sample with the smallest grain size (i.e. 50 nm SWCNT film MMC) strongly suggests that the composite exhibits different performance due to changes in the Ag-SWCNT layer interactions. Specifically, the SWCNT films have nanoscale porosity which will affect the resulting composite structure during the Ag over-coat, leading to greater tortuosity with increasing film thickness. Thus, the extent of Ag penetration through the SWCNT film to interact with the bottom Ag layer will be greatest for the 10 and 20 nm SWCNT films compared to the 50 nm film. Therefore, the observed deviation from Hall-Petch behavior for SWCNT film thicknesses between 20 and 50 nm suggests that Ag layer interactions are limited, leading to a transition from reinforcement to discrete layers in the MMC.

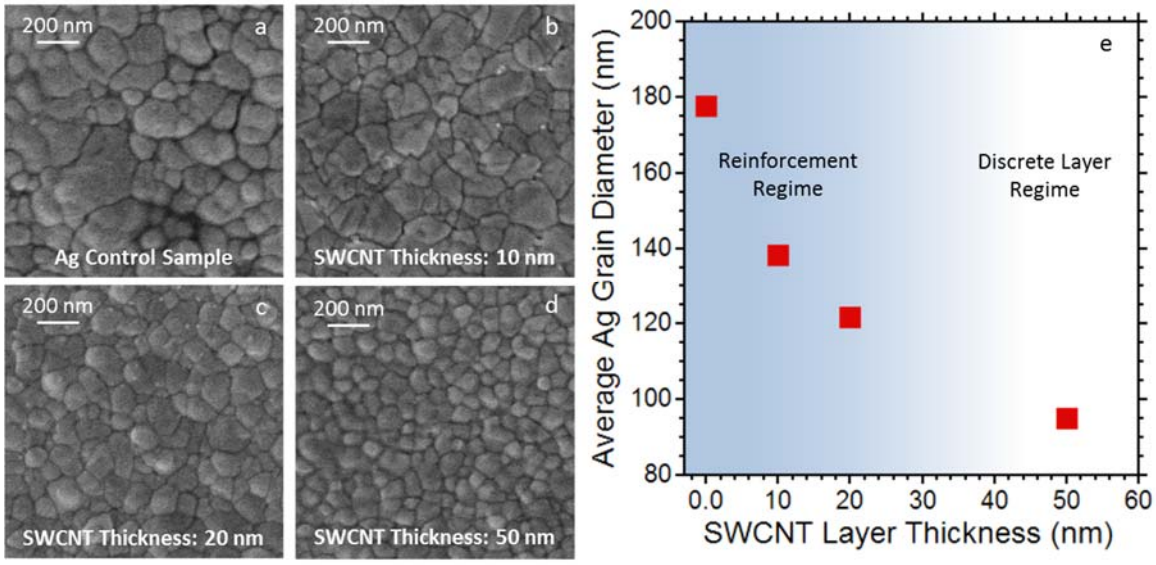

Figure 9. SEM micrographs of the Ag top-layer for (a) Ag control and MMC free-standing films with SWCNT layer thicknesses of (b) 10 nm (c) 20 nm, and (d) 50 nm. (e) The average Ag grain diameter as a function of SWCNT layer thickness.

Note: The labels and fading blue background indicate a transition from reinforcement to discrete layers

Further SEM analysis was conducted to examine the fracture edge of the FSFs after being stressed to failure (Figure 10). The SWCNTs protrude more than 1 μm from the fracture edge for the MMC samples, and the number of protruding SWCNTs increases with SWCNT layer thickness (Figure 10b-d). Additionally, the Ag top-layer delaminates for the structure containing a 50 nm SWCNT film, curling back to form a ridge along the fracture edge (Figure 10d). The delamination is not observed in the MMCs with lower SWCNT loading, further confirming the previous analysis of discrete layering occurring in the structure with 50 nm SWCNT films. The SEM analysis of the fracture edge suggests that embedded SWCNTs show strong potential to mechanically and electrically bridge micro-cracks in MMC electrodes for various applications such as solar cells and flexible electronics.

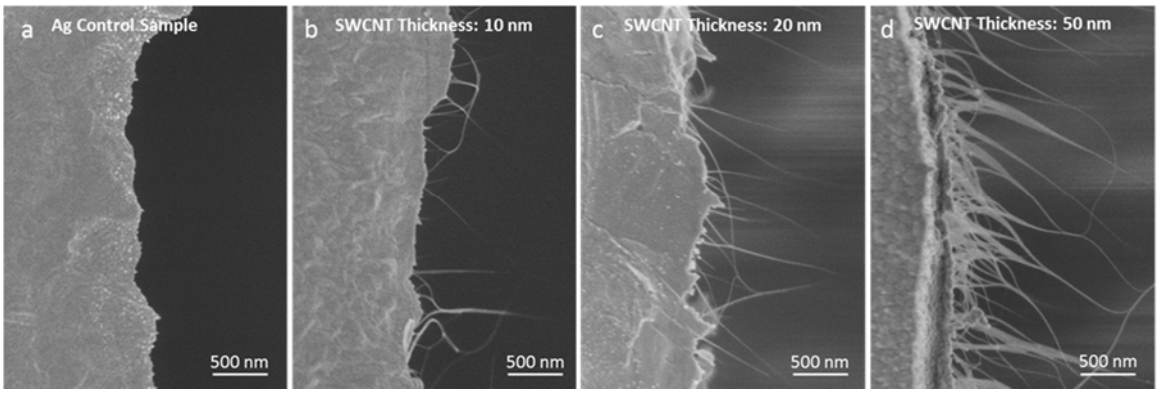

Figure 10. SEM micrographs of the fracture edges after tensile testing of (a) Ag control and MMCs with SWCNT layer thicknesses of (b) 10 nm (c) 20 nm, and (d) 50 nm.

Note: SWCNTs are shown protruding from the fracture edges

4.4 Conclusions

An innovative method was used to fabricate free-standing Ag-SWCNT MMC thin films and the resulting films were characterized to understand their response to applied tensile stress. Improvements in mechanical properties of the MMCs occurred as the SWCNT layer thickness was increased to 20 nm, exhibiting a 2.5x increase in toughness. Higher SWCNT loadings led to degradation in performance. SEM analysis and mechanical results suggest that the MMCs transition from a reinforced structure to discrete layers between 20 nm and 50 nm SWCNT layer thicknesses. The highest performing MMC with 20 nm SWCNT layer corresponds to ~0.7 vol. % SWCNTs in the composite. The SEM analysis shows evenly distributed SWCNTs protruding from the fracture edges, which would likely prevent catastrophic failure under less dramatic stresses. This work provides the important first step toward understanding the optimum SWCNT loading in the MMCs and provides a fundamental basis for which further studies can expand and develop additional improvements for advanced MMC electrodes.

5 CNT-MMC ELECTRICAL CHARACTERIZATION

5.1 Fabrication of SWCNT-MMC Grid Finger Structures

Measuring improved electrical performance of CNT-MMCs under mechanical stress (as compared to traditional Ag electrodes) is another important step toward demonstrating the utility of the MMCs as a more crack-resistant electrode. An apparatus was built at the Air Force Research Labs at Kirtland Air Force Base, New Mexico that measures the electrical resistance across cleaves and cracks (or "RACK") in order to mimic micro-crack propagation and thermal expansion scenarios. The RACK test apparatus is shown in Figure 11. The RACK testing is implemented by mounting grid finger structures on a printed circuit board (PCB) with a fixed end, a gap, and the opposing end attached to a stage driven by a piezo-electric motor. The MMC structures are scribed and cleaved across the PCB gap and the initial crack length is measured by optical microscopy. After the crack is initiated and measured, a piezo motor is activated, slowly widening the gap in the PCB board and recording the motor position, which, when combined

with the initial crack length, gives the total crack length. Load resistors (R1, R2, R3, R4) 200 Ω each are soldered to each grid finger, along with leads at the end of each grid finger and the bus bar, creating the circuit. The resistance of each grid finger is monitored for the duration of the mechanical testing until electrical failure, by monitoring the current and voltage drop across each grid finger and calculating the resistance from Ohm's law.

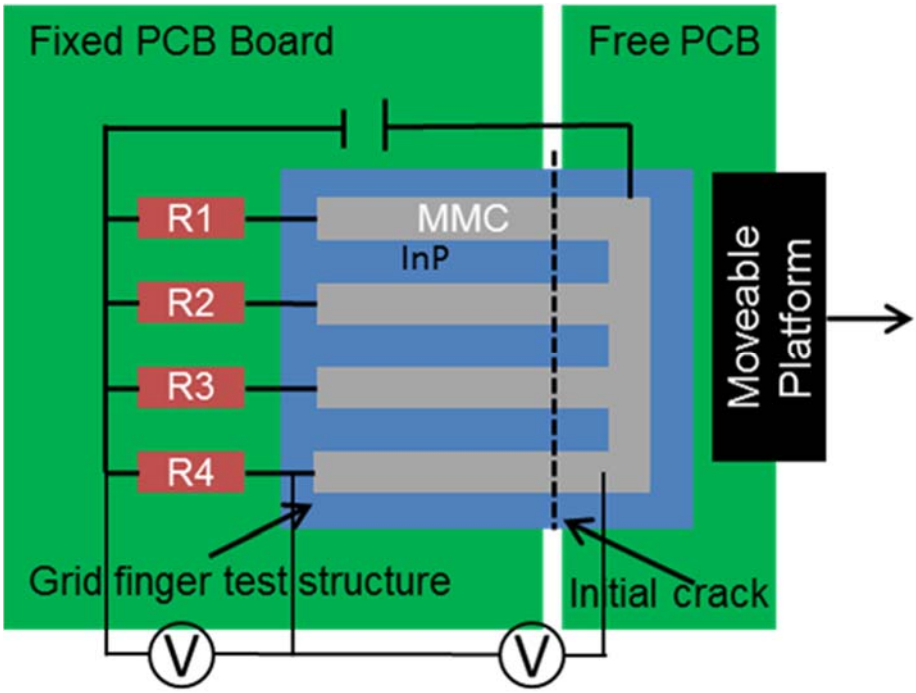

Figure 11. "RACK" electrical test fixture for testing grid finger MMC test structures.

Note: The dashed line in Figure 11 indicates the initial crack, which is followed by motion of the "free PCB" end. Load resistors (R1-R4) and electrical leads are attached for monitoring the grid finger electrical resistance during testing

Initial grid finger structures were fabricated for "RACK" testing to compare Ag to SWCNT-MMC electrode electrical performance. A grid finger shadow mask was designed and machined for deposition of the Ag grid finger layers. The design is shown in Figure 12a and a photograph of the final machined shadow mask is shown in Figure 12b. Following standard cleaning of the indium phosphide (InP) substrates with acetone and isopropyl alcohol (IPA), a Ti/Ag base-layer (5nm/500nm) was deposited through the grid finger mask. The complete sample set consisted of MMCs with SWCNT loadings of 1 $\mu g/cm^2$, 2 $\mu g/cm^2$, 5 $\mu g/cm^2$, and 10 $\mu g/cm^2$, along with Ag control samples. The SWCNT films were transferred by the standard MCE transfer process, and a photograph of the SWCNT films on Ag are shown in Figure 13.

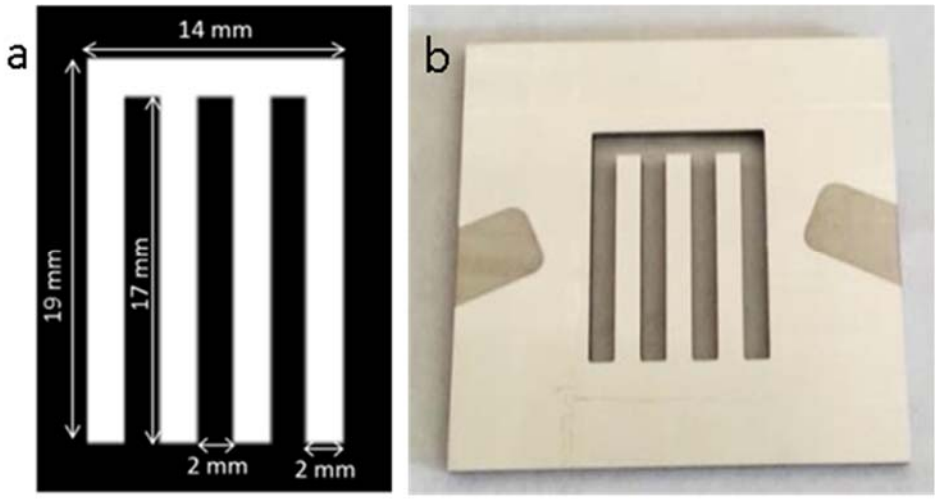

Figure 12. Grid finger shadow masks were designed for RACK electrical testing. (a) The design and dimensions of the grid finger mask. (b) A photograph of the finished grid finger mask

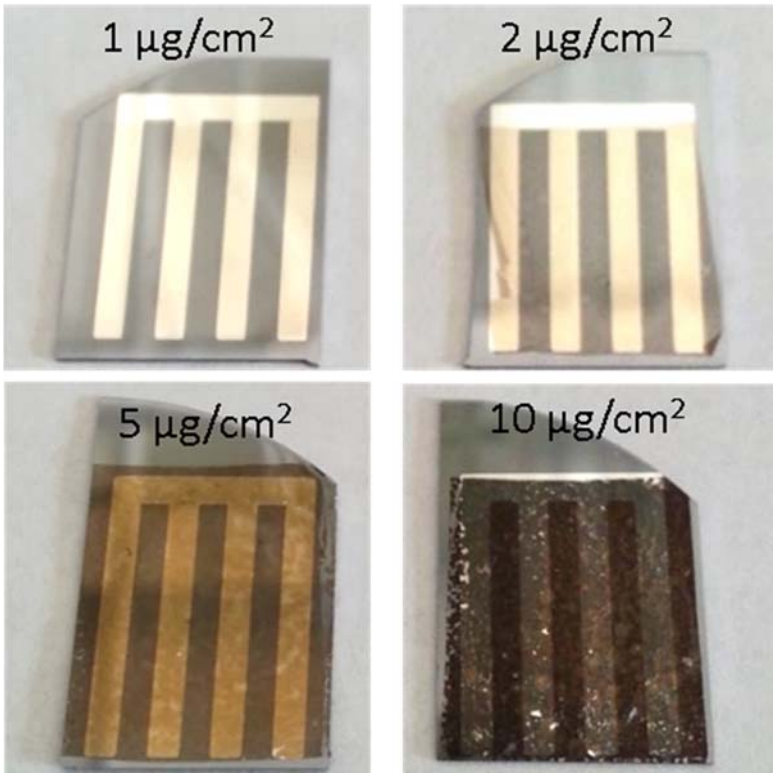

Figure 13. SWCNT films of varying areal density deposited onto Ti/Ag grid finger base-layers for RACK electrical testing

Ag top-layer deposition was performed subsequent to SWCNT film transfer by re-aligning the grid finger mask to the Ag base-layer (alignment verified by optical microscopy) and thermally evaporating 500 nm Ag through the shadow mask. At this step in the process, the MMC fabrication is complete; however, in order to create electrically isolated grid fingers, the

SWCNTs between the grid fingers need to be removed. A schematic illustrating the lithography and etch process for removing the SWCNTs in the field region is shown in Figure 14. Briefly, the cross-section is shown of the MMCs with SWCNTs in the field region (between the grid fingers). The entire structure is spin-coated with photoresist (Shipley S1813) and a clear field lithography mask is exposed using a broadband mercury lamp contact aligner (Karl Suss MA56, g-line) at 90 mJ/cm^2. Following exposure, the structures are developed in CD26 for 3.5 minutes, leaving the SWCNTs in the field region exposed and the grid finger portions masked by photoresist. The structures are then subjected to reactive ion etching (Drytek Quad RIE) in an oxygen plasma for 90 seconds, which etches the SWCNTs in the field region. Reactive ion etch conditions were 50 sccm O_2 flow rate, 100 mTorr chamber pressure, and 100 W RF power. It is important to note that the oxygen plasma also etches the photoresist, but calibrations of the etch rate under these conditions revealed that the SWCNTs are etched much more rapidly than the photoresist, so the Ag grid fingers remain protected from oxidation. The final step in the process is stripping the remaining photoresist from the electrodes, which is performed by soaking the structures in acetone for several minutes, followed by rinsing with acetone and IPA. The structures were shipped to the Air Force Research Laboratory for testing following successful completions of the fabrication process.

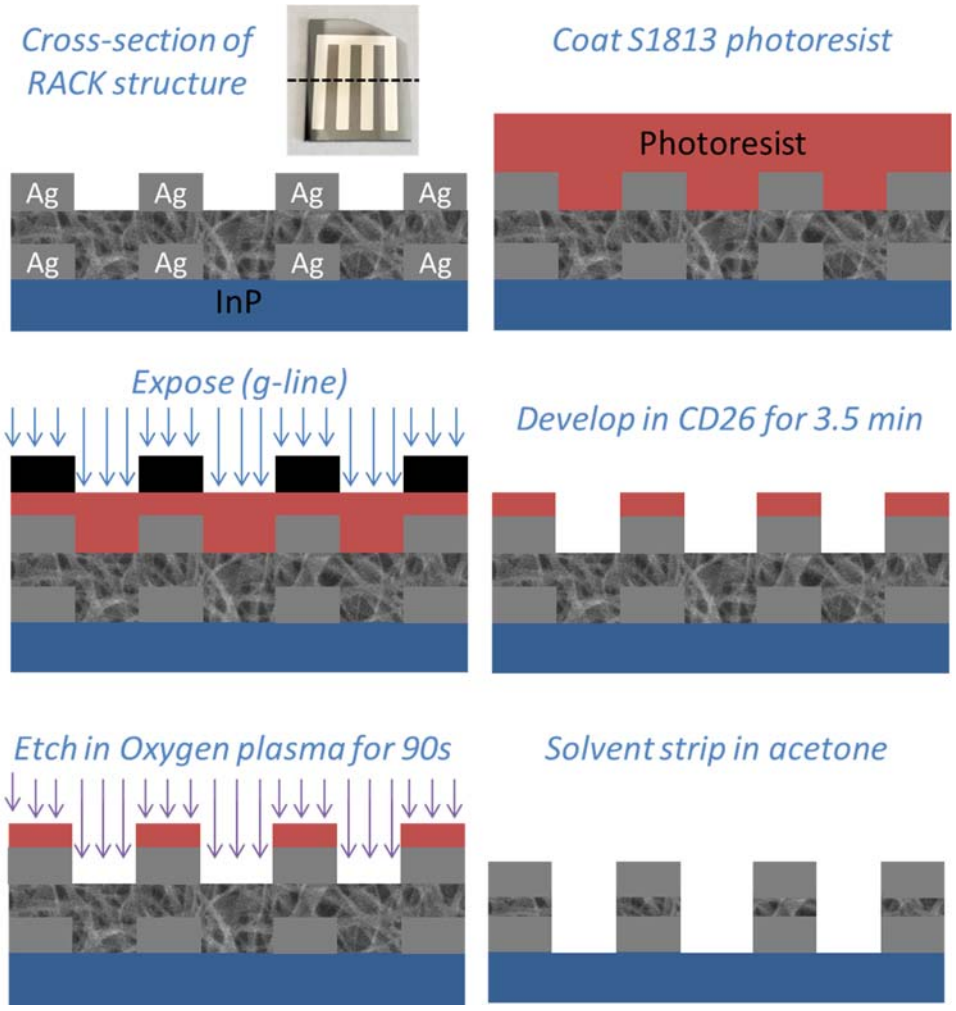

Figure 14. Schematic showing the lithography process flow for etching CNTs between grid fingers for electrically isolated structures

5.2 SWCNT-MMC Electrical Characterization

The samples described in section 5.1 were mounted on the RACK and tested using the procedure outlined in Figure 11. For the initial RACK tests, all Ag samples and many of the SWCNT MMC samples failed electrically at the initial crack. This is partly due to the need to develop a more controlled substrate fracture method, as the initial crack can vary from 2 µm to > 6µm. An example of RACK data for two SWCNT-MMC electrodes is shown in Figure 15, as the electrical resistance vs gap width. The pre-crack resistance was beyond the measurement capabilities of the instrumentation; consequently, a value of 0.135 Ω was assigned as the starting resistance, based on the geometry of the sample and the resistivity of pure bulk Ag (1.6×10^{-6} Ωcm)[36]. The 10 µg/cm^2 SWCNT-MMC maintains electrical connection at the initial fracture, with the resistance increasing only by ~2.5x at a crack width of ~2.8 µm. As the gap widens, the resistance increases minimally by ~3.4x (0.46 Ω) before failing electrically at a total gap width of ~5.5 µm. This is representative of the successful SWCNT-MMC samples, which generally maintained their electrical performance for gap widths up to ~6 µm. The proof of concept images of SWCNTs bridging gaps of ~3 µm (Figure 1) are thus consistent with the electrical test data.

The notable exception was one of the grid fingers on the 2 µg/cm^2. For this sample, the resistance increased by ~4.5x at the initial crack length of 5.57 µm. After the initial crack, the sample maintained fairly consistent electrical performance, increasing by another 4x (2.91 Ω) up to a gap width of ~11 µm. The fact that this sample outperforms all other samples is consistent with the free-standing film mechanical data, in which the highest toughness was observed in the 2 µg/cm^2 samples. Based on the trends in mechanical data, it is proposed that at the initial crack, the small increase in resistance is due to partial or complete failure of the Ag. The change in resistance also depends on the length of the initial crack, with larger changes in resistance observed for larger initial crack length. As the gap in the electrode increases, the resistance increases due to fewer SWCNTs available to bridge the gaps. The resistance remains in the mΩ range for all samples under 6 µm, and in the case of the best performing sample, the resistance remains in the single Ω range even at gaps of over 10 µm. Thus, the SWCNTs may be capable of maintaining adequate performance in the event of solar cell fractures, provided that the fractures are not larger than 5 – 10 µm.

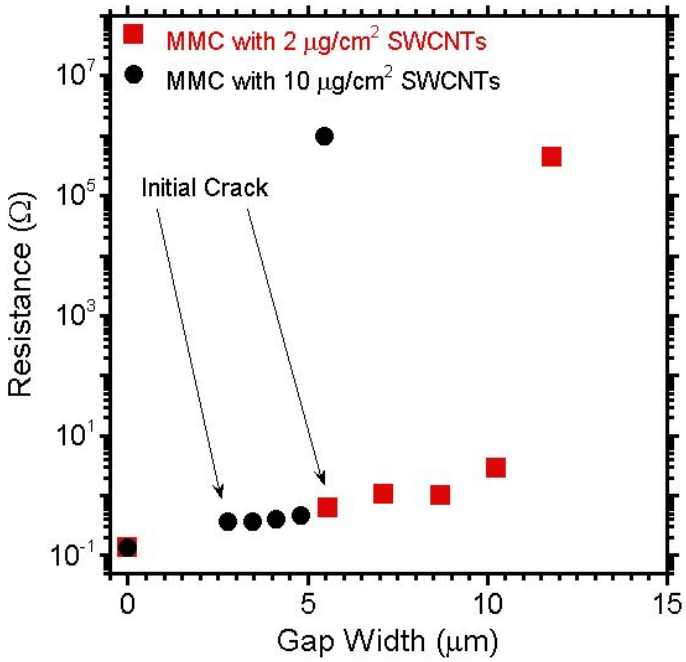

Figure 15. Results of RACK electrical testing showing the resistance versus gap width for MMCs with 2 µg/cm^2 and 10 µg/cm^2 SWCNT layer weight loadings

5.3 MWCNT-CNT Fabrication and Electrical Testing

Although the initial electrical, SEM, and mechanical results show an improvement for SWCNT-MMCs as compared to Ag-only electrodes, the incorporation of CVD MWCNTs into the MMCs may extend the crack bridging capabilities of the structures, as MWCNTs are typically much longer than SWCNTs. Figure 16a and b show MWCNT films of 5 µg/cm^2 and 20 µg/cm^2, respectively. The MWCNTs have much larger diameters than the SWCNTs, which changes how the MWCNTs pack together into a film. Thus, the MWCNT films have much more void space and height than SWCNT films with equivalent areal densities, as confirmed by

profilometry and SEM measurements. SEM analysis reveals that successive depositions of Ag top-layer up to 4 µm is not sufficient to fully encapsulate the MWCNTs, despite filling of the void space in the 5 µg/cm^2, as shown in Figure 16c and d. This thickness of Ag is approaching the upper limit for solar cell electrode thickness; therefore, no additional Ag was deposited.

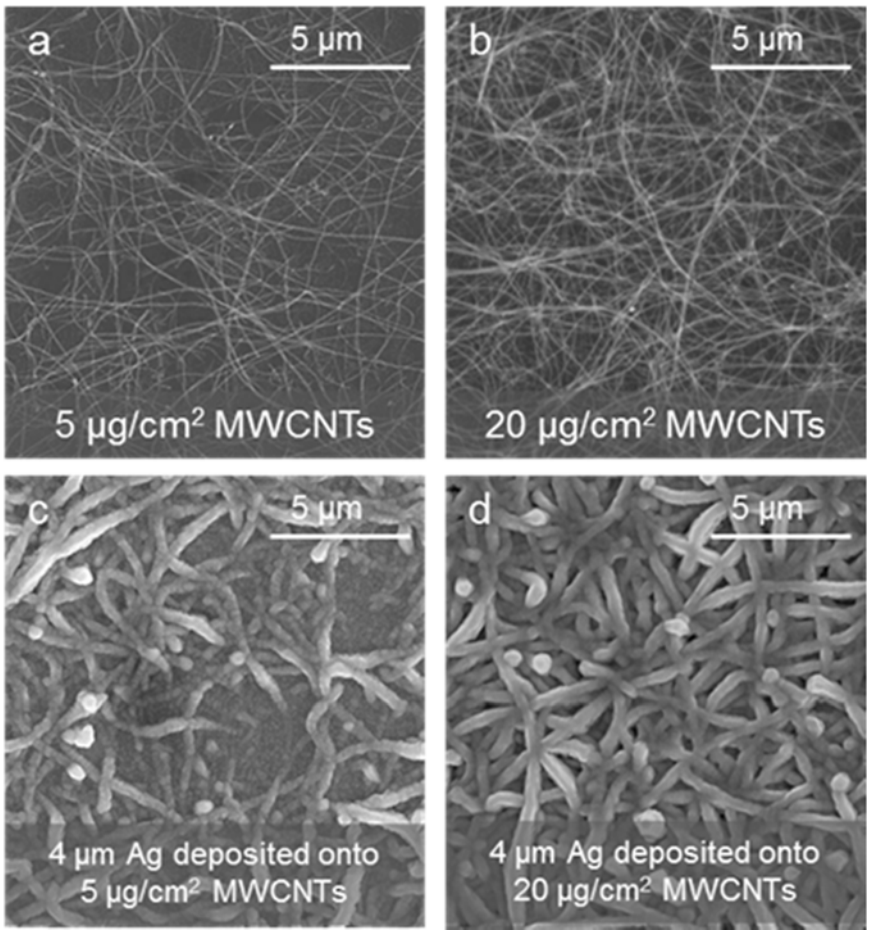

Figure 16. SEM images of as-deposited MWCNT films with areal densities of (a) 5 µg/cm2 and (b) 20 µg/cm2, and over-coated with 4 µm of evaporated Ag

SEM analysis was also performed to assess the ability of the MWCNTs to mechanically bridge gaps caused by substrate fracture. Figure 17 shows a representative SEM of a MWCNT-MMC, with the MWCNTs bridging a gap of ~15 µm, and other samples exhibited similar bridging, up to 40 µm.

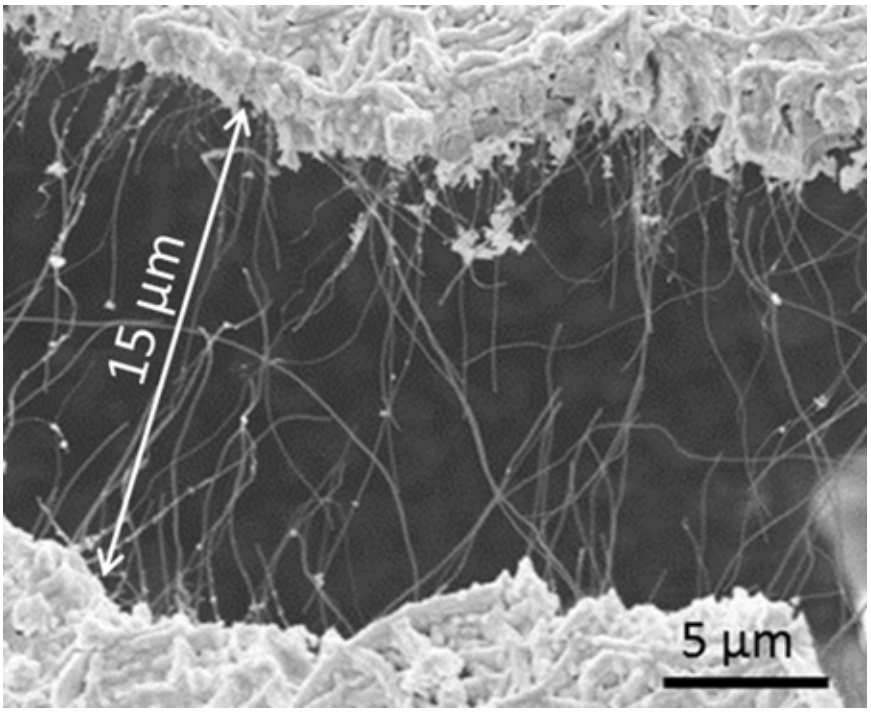

Figure 17. SEM images of a MWCNT-MMC showing MWCNTs bridging a gap in the Ag of ~15 µm

Despite the inability to fully encapsulate the MWCNTs in Ag, the SEM analysis clearly indicates that MWCNTs can span much larger gaps than the shorter SWCNTs. Thus, MWCNT/SWCNT "hybrid" films were used in fabricating test structures for further RACK electrical testing. Two samples were fabricated with SWCNT/MWCNT ratios of 80%/20% and 20%/80%, by weight, with CNT film areal densities of 5 µg/cm^2. Although SWCNT-MMCs with 2 µg/cm^2 SWCNT performed the best in both mechanical and electrical testing, an areal density of 5 µg/cm^2 was chosen for the SWCNT/MWCNT hybrid MMCs because of the increased void space caused by the large MWCNT diameter, which was previously addressed in the discussion of Figure 16a and b. A representative RACK electrical data set for each sample is shown in Figure 18. The 80% SWCNT sample exhibits a 2x increase in resistance upon initial fracture of 1.73 µm, while the 20% SWCNT sample exhibits an 11x increase at an initial fracture of 2.22 µm. The 11x increase in resistance is also higher than that observed in Figure 15 for a similar initial fracture, which resulted in only ~2x increase in resistance. This more significant increase in resistance for the 20% SWCNT sample is likely due to the fact that there are less SWCNTs to bridge the initial fracture. As the gaps are widened to ~5 µm, both samples exhibit an increase in resistance by an order of magnitude to between 50 and 70 Ω, which further supports that the SWCNTs are able to maintain reasonable electrical performance when fractures are less than ~6 µm. However, the resistance at this gap extension is larger than the resistance of the pure SWCNT-MMCs at roughly the same gap width (as shown in Figure 15). It is proposed that SWCNTs can still provide electrical pathways, but as they are randomly dispersed and entangled within the MWCNT network, the number of pathways composed purely of SWCNTs decreases. Put another way, the SWCNT network is likely below the percolation threshold for maintaining electrical resistance in the single Ohms. This is also consistent with observations that there will

be higher resistance at CNT junctions, and this resistance will increase with increasing heterogeneity.

Above a 5 µm gap width, the resistance of each sample increases to the kΩ range at an extension of ~10 µm. Beyond 10 µm gap width, the samples both increase in resistance until electrical failure at an extension of ~28.5 µm. All other grid fingers for both samples also consistently failed electrically between 20 and 30 µm. Despite the similar performance, the 80% SWCNT sample does experience more significant increases in resistance as the gap widens. This is likely due to the fact that the less conductive MWCNTs are providing a majority of the electrical and mechanical bridging above 10 µm gap widths, but that there are much fewer of them to contribute to the conduction than in the 20% SWCNT sample. Overall the results show that the addition of MWCNTs provides mechanical and electrical connection at much longer gap widths than the previous tests with SWCNTs-only. However, from an application perspective, a resistance of kΩ is not appropriate for a solar cell electrode, and therefore strategies to increase the MWCNT loading or conductivity would be necessary to facilitate the desired performance for larger gaps.

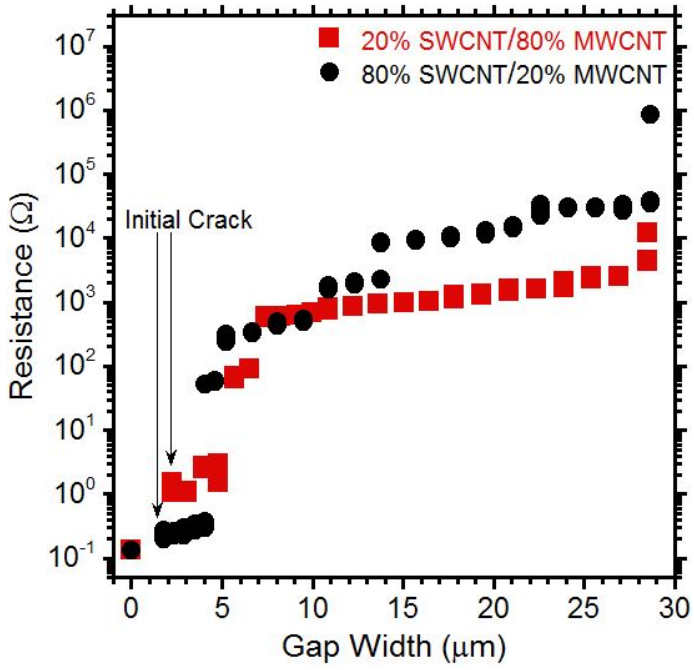

Figure 18. Electrical resistance versus total gap width for SW/MW-MMC electrodes with SWCNT/MWCNT weight ratios of 20%/80% and 80%/20%

5.4 Additional MWCNT-MMC Development

The positive results from the electrical testing of MWCNT-MMC RACK test structures warrants further exploration of MWCNTs as an addition or alternative to the SWCNTs as reinforcement material. However, it was decided that the CVD MWCNTs used for the RACK electrical demonstration were not suitable as a reinforcement material due to their large diameters, which made it difficult to fabricate films at low areal densities and also made it

difficult to encapsulate with over-coated Ag. Thus, RIT investigated potential MWCNT candidates from commercial sources as a viable replacement for the CVD MWCNTs. The as-received MWCNTs were characterized via Raman spectroscopy, thermogravimetric analysis (TGA), and SEM to assess their potential to replace the CVD MWCNTs.

MWCNTs were purchased from cheaptubes.com, and the results of the characterization of the as-received material are shown in Figure 19. The TGA in Figure 19a shows a single decomposition at 595 °C and 4.4% residual mass, indicating little carbonaceous impurities or metal catalysts remaining from synthesis. The SEM (Figure 19b) confirms the MWCNTs are relatively clean and free from impurities; however, curvature and kinks in the MWCNTs are indicative of defects. The Raman spectra in Figure 19c shows the characteristic D, G, and G' peaks related to MWCNTs; the D peak is related to defects and the G and G' peaks are related to graphitic sp^2 bonds. The Raman spectrum clearly shows high D/G and D/G' peak ratios, indicating relatively high number of defects. Furthermore, after being filtered into a film, transferred to a substrate, and subsequently thermally oxidized to remove impurities from filtration, the MWCNT areal density significantly decreased, further confirming the defective nature of the MWCNTs. Thus, the MWCNTs from cheaptubes.com were determined to be unsuitable for incorporation into MMCs.

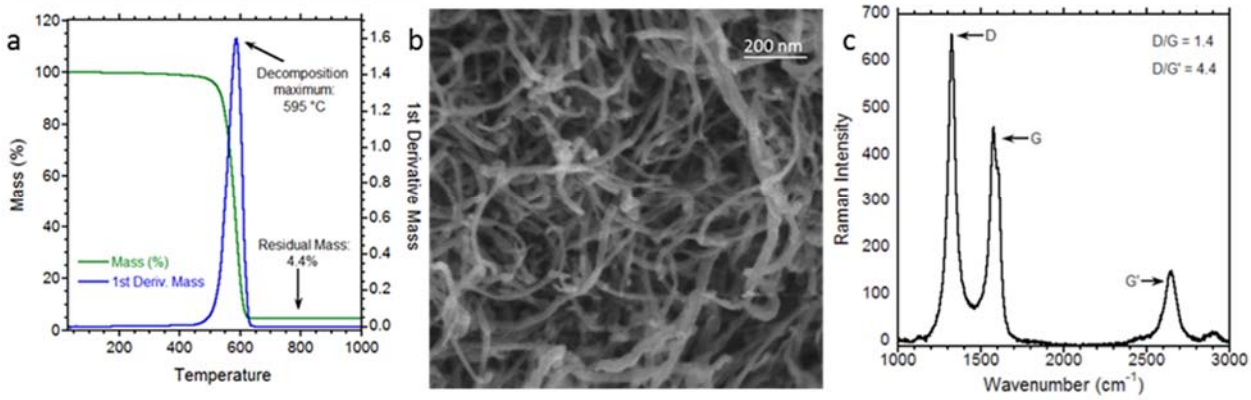

Figure 19. MWCNTs from cheaptubes.com were characterized via (a) thermogravimetric analysis, (b) SEM, and (c) Raman spectroscopy

MWCNT sheet soot was also acquired from Nanocomp Technologies Inc. (NCTI) for possible use in future MMCs. The soot typically contains a high level of amorphous carbon and iron catalyst impurities, so the thermal oxidation and HCl treatment discussed in section 4.2 was performed to purify the soot. The TGA curves are shown in Figure 20 for both as-received and purified MWCNT soot. TGA of the as-received soot (Figure 20a) shows a shoulder which indicates two decompositions, likely due to amorphous carbon and MWCNTs, along with ~42% residual mass from catalyst particles and other impurities. After purification, a single decomposition peak is observed in Figure 20b with a residual mass of only ~4.2%, indicating effective removal of amorphous carbon during thermal oxidation and of metal catalysts during HCl purification. The Raman spectrum in Figure 20c shows low D/G and D/G' peak ratios, indicating much lower relative defect content than that observed for the MWCNTs from cheaptubes.com.

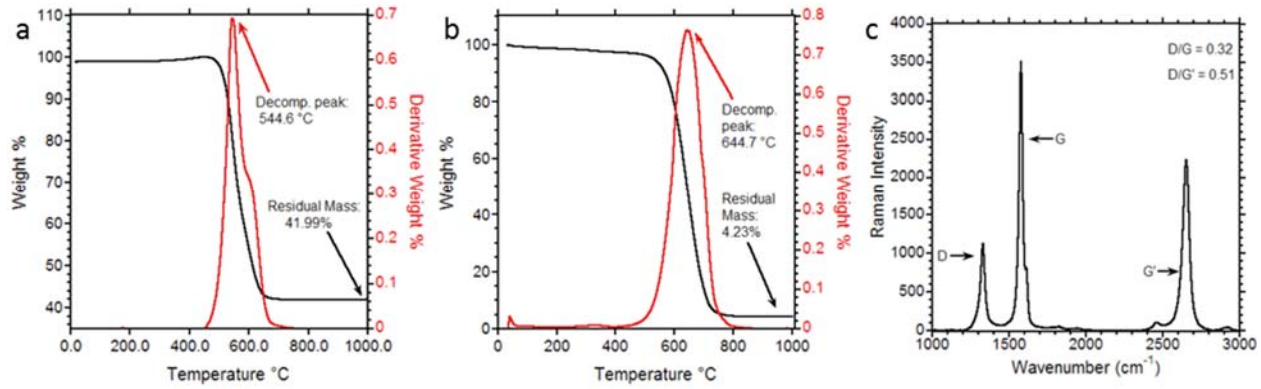

Figure 20. Material characterization of MWCNTs from NCTI. The TGA is shown for (a) as-received and (b) purified MWCNT soot, as well as (c) the Raman spectrum for the purified soot

Purified NCTI MWCNT films were filtered onto an MCE membrane from a 2 wt% SDS dispersion and deposited onto InP by the standard MCE transfer process at varying areal densities, followed by SEM analysis. Figure 21 shows two of the resulting MWCNT films at 2.75 µg/cm^2 (Figure 21a) and 5 µg/cm^2 (Figure 21b). Void space is observed in the MWCNT films, which decreases with increasing areal density. As discussed previously, some void space may be desirable from the perspective that this will enable the Ag top and bottom layers to interact and make a more cohesive composite. From the SEM images, it is clear that the NCTI MWCNTs are much straighter and longer than the cheaptubes.com MWCNTs. The NCTI MWCNT diameter was found to be ~20 ± 10 nm by *>400 ImageJ* measurements, giving a significant advantage over the previous CVD MWCNTs, which had diameters ranging from 50 to 150 nm. Thus, the MWCNTs from NCTI were selected as the best MWCNT candidate for MWCNT MMCs moving forward.

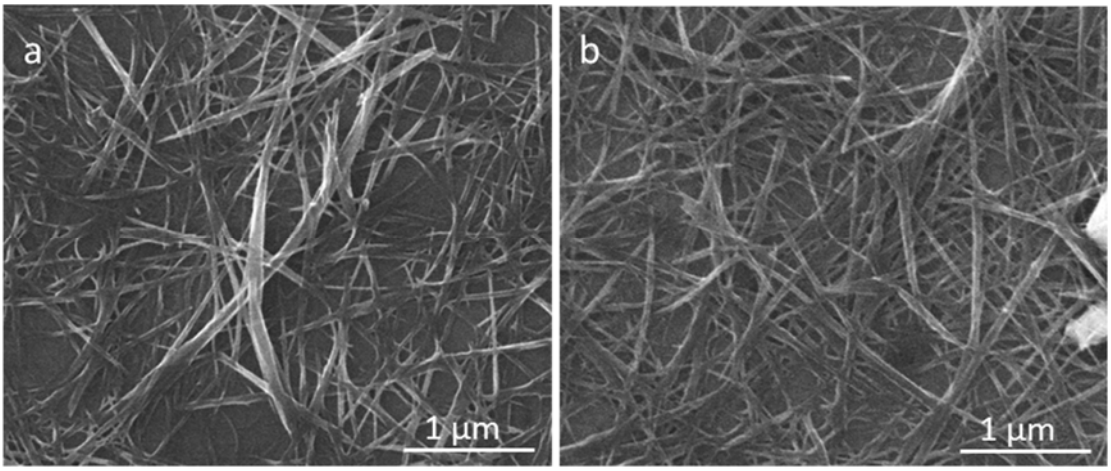

Figure 21. SEM images of films fabricated from the purified NCTI MWCNT soot material and transferred to InP substrates at areal densities of (a) 2.75 µg/cm^2 and (b) 5 µg/cm^2

5.5 Conclusions

Fabrication processes and electrical testing procedures have been developed for assessing the electrical performance CNT-MMC grid finger structures under stress. The grid finger structures utilized SWCNTs, MWCNTs, or combinations thereof, and the processing techniques were all compatible with standard microelectronic engineering processes. The results of electrical testing and SEM analysis of the MMCs under stress suggest that SWCNT-MMC electrodes give an advantage over pure Ag electrodes. The SWCNTs are limited in crack-bridging capabilities, but are able to maintain electrical performance up to ~6 μm gap widths due to SWCNT length. Incorporation of much longer MWCNTs into the SWCNT-MMCs results in ~4× to 5× increase in crack-bridging capabilities, which may be useful if it is found that some solar cell or flexible electronics applications suffer from gaps larger than 6 μm. Additionally, assessment of an alternative to the large-diameter CVD MWCNTs used in the initial hybrid RACK electrical tests resulted in the selection of MWCNT materials from Nanocomp Technologies, Inc., which had small diameters, low defect content, and responded positively to traditional chemical and thermal purification techniques. This work represents a significant step toward realizing more robust electrodes.

6 CNT-MMC INTEGRATION INTO SOLAR CELLS

6.1 Introduction

Although the funding was not provided for the 3rd year, RIT had begun at the end of the 2nd year to evaluate the implementation of the CNT MMCs onto state-of-the-art triple junction solar cells (ZTJ) provided by SolAero. The preliminary findings are discussed in the section that follows, which includes the process flow for fabrication and application of MMC grid fingers to the ZTJ cells, as well as some initial testing under simulated light conditions for air mass zero (AM0).

6.2 Fabrication Process Flow

The SolAero triple-junction solar cells (ZTJ) were shipped to RIT coated in photoresist, which was exposed and developed such that a seed metal layer (for electrodeposition) defining the grid finger contacts was exposed. The solar cells were essentially completed otherwise, with the anti-reflective coating and back contact metallization complete. Because RIT's MMC fabrication process utilizes thermal evaporation for the Ag, a different process was needed to apply the MMC grid finger contacts; thus, the photoresist was solvent stripped and RIT designed and commissioned new lithography masks for a metal liftoff process for the grid finger metallization. A condensed fabrication process flow for applying the CNT-MMCs to the SolAero ZTJ cells is shown in Figure 22. The process starts by stripping the photoresist, leaving the seed metal grid fingers intact, as shown in step 1. The sample is coated in a liftoff resist and another layer of standard positive photoresist (S1813) in step 2, exposed at 365 nm (step 3), and developed in CD 26 developer, leaving the exposed liftoff "pits" as shown in the cross-section in step 4. The Ag layer (1 μm) is then deposited via thermal evaporation and the photoresist stripped with Remover PG, leaving the first MMC metal grid finger layer, as shown in step 5. CNT films are transferred using the MCE transfer process described previously (step 6). Following CNT film transfer, the CNTs in the field region are etched away via an O_2 plasma etch in steps 7-10, as described previously in section 5.1 and Figure 14, leaving the structures as shown in step 11. The metal liftoff is repeated (steps 2-5), leaving the final structure shown in step 12. Figure 23 contains camera images showing the MWCNT film transferred to the solar cell surface (step 6), and the final structure (step 12) after the CNT plasma etch and final Ag liftoff have been performed.

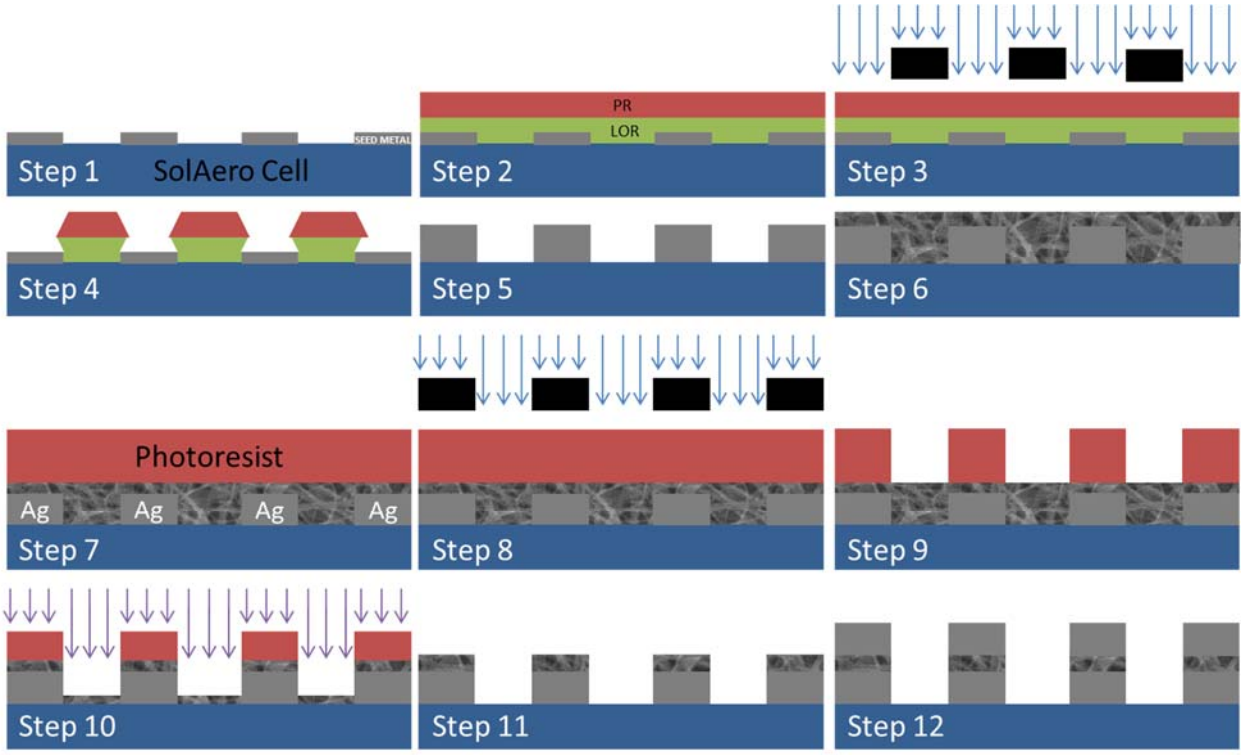

Figure 22. Schematic showing a cross section of a condensed fabrication process flow for applying CNT-MMC electrodes to SolAero ZTJ solar cells

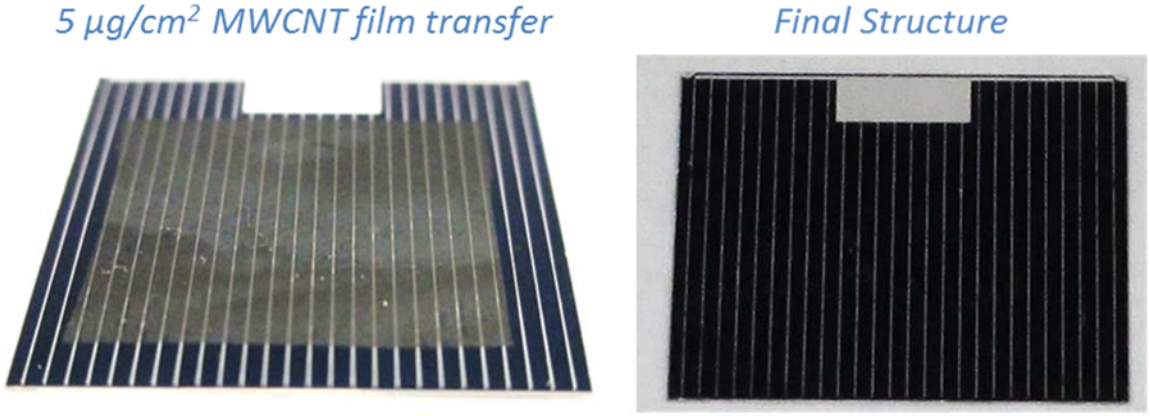

Figure 23. Camera images showing a SolAero ZTJ cell with a MWCNT film transferred to the surface and the final structure after etching the CNTs and performing the final Ag liftoff

6.3 Solar Cell Testing

The finished set of SolAero cells with integrated CNT-MMC top-contacts consisted of a sample with pure Ag (control), a sample with 5 µg/cm^2 NCTI MWCNTs, and a sample with 2 µg/cm^2 SWCNTs (synthesized at RIT). The samples were characterized in a solar simulator under AM0 illumination conditions. Figure 24a shows the current-voltage (I-V) curves for the

MWCNT sample. The as-fabricated sample (black line on plot) lacks typical solar cell I-V characteristics due to major shunt resistance problems, which was common to all three samples upon initial testing. Gently cleaning the edges of the cells with fine sandpaper as shown in Figure 24b caused recovery of the I-V characteristics as shown by the red curves, indicating shorting of top and bottom cells was alleviated. The source of the electrical short remains unknown; however, this is likely not an issue as the cells would not typically be cleaved prior to top contact metallization in an industrial fabrication process.

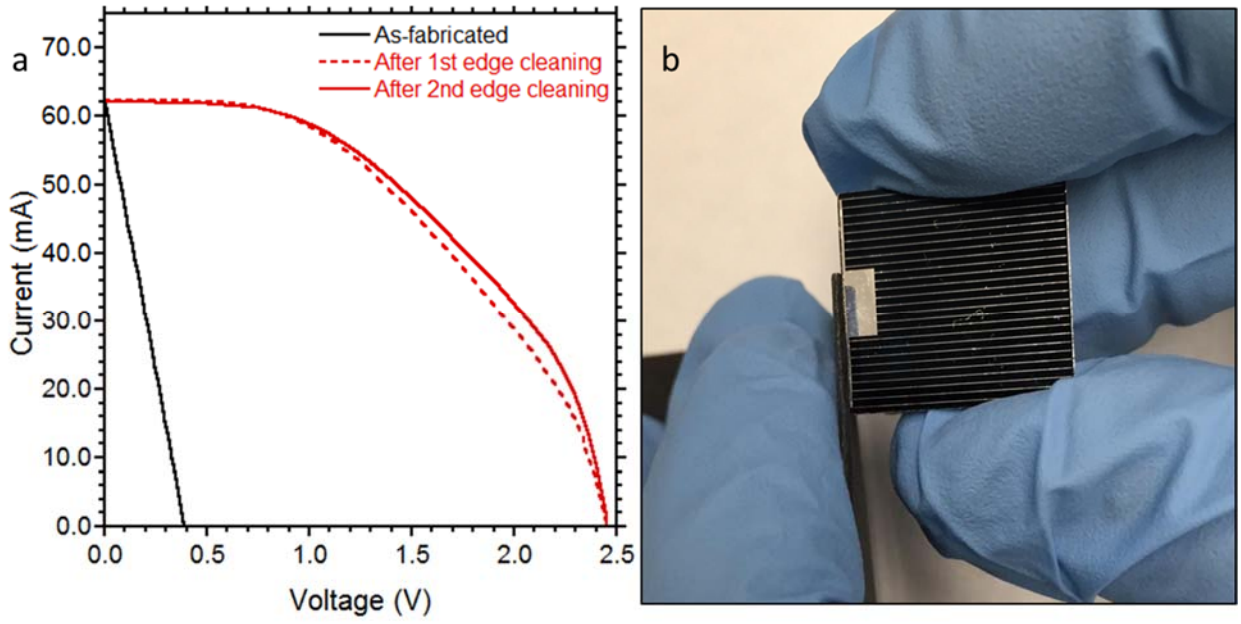

Figure 24. The figure shows (a) I-V curves for the MWCNT sample, both as-fabricated and after a gentle edge cleaning with sandpaper, which is depicted in (b) the image on the right

After gently cleaning the sides of each solar cell with sandpaper, the AM0 electrical testing was conducted for all three samples. The results of the I-V tests under AM0 simulated light conditions are shown in Figure 25, and the performance metrics calculated from the IV curves are shown in Table 1 where the first column shows the specification sheet data provided by SolAero for a typical 3rd generation triple junction (ZTJ) performance. Cells performed relatively well, operating at ~90% of the J_{sc} specification and just below the V_{oc} specification. The efficiency was significantly less than the 29% specification, but did reach 22% for the SWCNT-MMC sample. The fact CNT MMCs equal or exceed the performance of the Ag control sample indicates that the performance issues are likely addressable by refining lithography, metallization, and CNT etch processes. In observing the edges via microscopy after cleaning with sandpaper, it was clear that some of the surface at the edges had been damaged by the sandpaper, which could also contribute to the decreased efficiency.

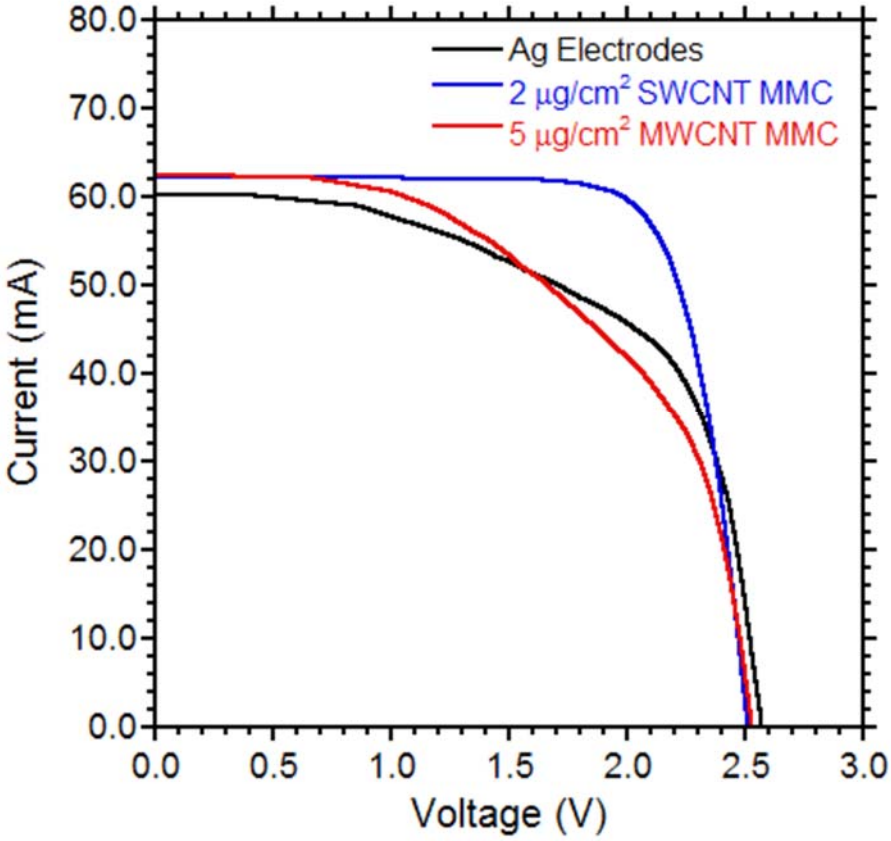

Figure 25. The final I-V curves for the SolAero cells with RIT's MMC contact metallization scheme, with a silver-only control sample, a 2 µg/cm^2 SWCNT MMC (blue), and a 5 µg/cm^2 MWCNT MMC (red)

Table 1. ZTJ specifications provided by SolAero and the measured values for each sample fabricated at RIT and tested under AM0 simulated light

	ZTJ spec sheet data	Ag-only control	2µg/cm^2 SWCNTs	5µg/cm^2 MWCNTs
J_{sc} (mA/cm^2)	17.4	15.1	15.6	15.6
V_{oc} (V)	2.7	2.6	2.5	2.5
Fill factor (%)	--	59.5	76.8	53.5
Efficiency (%)	29.5	16.9	22.0	15.4

7 CONCLUSIONS

The CNT MMC fabrication process developed by RIT has been applied to commercial space solar cells, with demonstrations of both MWCNT and SWCNT MMC electrodes. The as-fabricated cells all suffered from electrical shorting (between top and bottom cells) that was easily addressable by gently cleaning the edges with sandpaper, an issue that would not arise in standard production as the cells are not cleaved until after the top metallization is complete. The cells suffered from some loss of efficiency, but performed close to specifications for short-circuit current and open-circuit voltage. It is likely that the performance can be greatly improved by refining the lithography and other fabrication processes. Attempts to test the cells under fracture stress were unsuccessful due to difficulties in creating controlled cracks in the substrate, a task that would be addressed and completed in future work. This first attempt/success at integrating a fully clean room-compatible CNT-MMC fabrication process into state of the art triple junction space solar cells represents a very important step toward future adoption of the technology as a more robust electrode material. The implications extend beyond IMM devices to other solar markets, and even flexible electronics

REFERENCES

[1] S. Kajari-Schröder, I. Kunze, U. Eitner, and M. Köntges, "Spatial and orientational distribution of cracks in crystalline photovoltaic modules generated by mechanical load tests," *Solar Energy Materials and Solar Cells,* vol. 95, pp. 3054-3059, 11// 2011.

[2] M. Köntges, I. Kunze, S. Kajari-Schröder, X. Breitenmoser, and B. Bjørneklett, "The risk of power loss in crystalline silicon based photovoltaic modules due to micro-cracks," *Solar Energy Materials and Solar Cells,* vol. 95, pp. 1131-1137, 4// 2011.

[3] P. Chaturvedi, B. Hoex, and T. M. Walsh, "Broken metal fingers in silicon wafer solar cells and PV modules," *Solar Energy Materials and Solar Cells,* vol. 108, pp. 78-81, 1// 2013.

[4] T. H. Reijenga and H. F. Kaan, "PV in Architecture," *Handbook of Photovoltaic Science and Engineering, Second Edition,* pp. 1043-1077, 2011.

[5] R. M. France, *et al.*, "Pushing Inverted Metamorphic Multijunction Solar Cells Toward Higher Efficiency at Realistic Operating Conditions," *IEEE Journal of Photovoltaics,* vol. 3, pp. 893-898, Apr 2013.

[6] P. Patel, *et al.*, "Experimental Results From Performance Improvement and Radiation Hardening of Inverted Metamorphic Multijunction Solar Cells," *IEEE Journal of Photovoltaics,* vol. 2, pp. 377-381, Jul 2012.

[7] F. Newman, *et al.*, "PROGRESS IN ADAPTING INVERTED METAMORPHIC SOLAR CELL TECHNOLOGY FOR TERRESTRIAL CONCENTRATOR APPLICATIONS," in *PVSC: 2008 33rd IEEE Photovoltaic Specialists Conference,* San Diego, CA. *Vols 1-4*, ed, 2008, pp. 554-558.

[8] Y. Feng, H. L. Yuan, and M. Zhang, "Fabrication and properties of silver-matrix composites reinforced by carbon nanotubes," *Materials Characterization,* vol. 55, pp. 211-218, 2005.

[9] S. R. Bakshi, V. Singh, S. Seal, and A. Agarwal, "Aluminum composite reinforced with multiwalled carbon nanotubes from plasma spraying of spray dried powders," *Surface and Coatings Technology,* vol. 203, pp. 1544-1554, 2009.

[10] D. D. Phuong, *et al.*, "Effects of carbon nanotube content and annealing temperature on the hardness of CNT reinforced aluminum nanocomposites processed by the high pressure torsion technique," *Journal of Alloys and Compounds,* vol. 613, pp. 68-73, 2014.

[11] P. Gill and N. Munroe, "Study of Carbon Nanotubes in Cu-Cr Metal Matrix Composites," *Journal of Materials Engineering and Performance,* vol. 21, pp. 2467-2471, 2012.

[12] L. Shi, C. Sun, P. Gao, F. Zhou, and W. Liu, "Electrodeposition and characterization of Ni–Co–carbon nanotubes composite coatings," *Surface and Coatings Technology,* vol. 200, pp. 4870-4875, 2006.

[13] F. Li, H. Cheng, S. Bai, G. Su, and M. Dresselhaus, "Tensile strength of single-walled carbon nanotubes directly measured from their macroscopic ropes," *Applied Physics Letters,* vol. 77, pp. 3161-3163, 2000.

[14] D. A. Walters and L. M. Ericson, "Elastic strain of freely suspended single-wall carbon nanotube ropes," *Applied Physics Letters,* vol. 74, p. 3803, 1999.

[15] X. L. Shi, *et al.*, "Fabrication and properties of W–Cu alloy reinforced by multi-walled carbon nanotubes," *Materials Science and Engineering: A,* vol. 457, pp. 18-23, 2007.

[16] T. Laha and A. Agarwal, "Effect of sintering on thermally sprayed carbon nanotube reinforced aluminum nanocomposite," *Materials Science and Engineering: A,* vol. 480, pp. 323-332, 2008.

[17] T. Laha, S. Kuchibhatla, S. Seal, W. Li, and A. Agarwal, "Interfacial phenomena in thermally sprayed multiwalled carbon nanotube reinforced aluminum nanocomposite," *Acta Materialia,* vol. 55, pp. 1059-1066, Feb 2007.

[18] F. Wang, S. Arai, and M. Endo, "The preparation of multi-walled carbon nanotubes with a Ni–P coating by an electroless deposition process," *Carbon,* vol. 43, pp. 1716-1721, 2005.

[19] S. Arai, A. Fujimori, M. Murai, and M. Endo, "Excellent solid lubrication of electrodeposited nickel-multiwalled carbon nanotube composite films," *Materials Letters,* vol. 62, pp. 3545-3548, 2008.

[20] S.-m. Zhou, X.-b. Zhang, Z.-p. Ding, C.-y. Min, G.-l. Xu, and W.-m. Zhu, "Fabrication and tribological properties of carbon nanotubes reinforced Al composites prepared by pressureless infiltration technique," *Composites Part A: Applied Science and Manufacturing,* vol. 38, pp. 301-306, 2007.

[21] J. Y. Hwang, A. Neira, T. W. Scharf, J. Tiley, and R. Banerjee, "Laser-deposited carbon nanotube reinforced nickel matrix composites," *Scripta Materialia,* vol. 59, pp. 487-490, 2008.

[22] S. R. Bakshi, D. Lahiri, and A. Agarwal, "Carbon nanotube reinforced metal matrix composites - a review," *International Materials Reviews,* vol. 55, pp. 41-64, 2010.

[23] H. Espinosa, B. Prorok, and M. Fischer, "A methodology for determining mechanical properties of freestanding thin films and MEMS materials," *Journal of the Mechanics and Physics of Solids,* vol. 51, pp. 47-67, 2003.

[24] I. Chasiotis, C. Bateson, K. Timpano, A. McCarty, N. Barker, and J. Stanec, "Strain rate effects on the mechanical behavior of nanocrystalline Au films," *Thin Solid Films,* vol. 515, pp. 3183-3189, 2007.

[25] R. Emery and G. Povirk, "Tensile behavior of free-standing gold films. Part I. Coarse-grained films," *Acta Materialia,* vol. 51, pp. 2067-2078, 2003.

[26] M. Haque and M. Saif, "Deformation mechanisms in free-standing nanoscale thin films: A quantitative in situ transmission electron microscope study," *Proceedings of the National Academy of Sciences of the United States of America,* vol. 101, pp. 6335-6340, 2004.

[27] H. Huang and F. Spaepen, "Tensile testing of free-standing Cu, Ag and Al thin films and Ag/Cu multilayers," *Acta Materialia,* vol. 48, pp. 3261-3269, 2000.

[28] Z. Wu, *et al.*, "Transparent, conductive carbon nanotube films," *Science,* vol. 305, pp. 1273-6, Aug 27 2004.

[29] B. J. Landi, C. D. Cress, C. M. Evans, and R. P. Raffaelle, "Thermal oxidation profiling of single-walled carbon nanotubes," *Chemistry of Materials,* vol. 17, pp. 6819-6834, Dec 27 2005.

[30] B. J. Landi, H. J. Ruf, C. M. Evans, C. D. Cress, and R. P. Raffaelle, "Purity assessment of single-wall carbon nanotubes, using optical absorption spectroscopy," *Journal of Physical Chemistry B,* vol. 109, pp. 9952-9965, May 26 2005.

[31] J. E. Rossi, C. D. Cress, A. Merrill, K. J. Soule, N. D. Cox, and B. J. Landi, "Intrinsic diameter dependent degradation of single-wall carbon nanotubes from ion irradiation," *Carbon,* vol. 81, pp. 488-496, 1// 2015.

[32] N. D. Cox, J. E. Rossi, and B. J. Landi, "Carbon nanotube metal matrix composites for solar cell electrodes," in *Photovoltaic Specialist Conference (PVSC), 2015 IEEE 42nd*, New Orleans, LA, pp. 1-4, 2015.

[33] K. Wilson, E. V. Barrera, and Y. Bayazitoglu, "Processing of Titanium Single-Walled Carbon Nanotube Metal-Matrix Composites by the Induction Melting Method," *Journal of Composite Materials,* vol. 44, pp. 1037-1048, 2010.

[34] F. Louchet, J. Weiss, and T. Richeton, "Hall-Petch law revisited in terms of collective dislocation dynamics," *Physical Review Letters,* vol. 97, p. 075504, 2006.

[35] L. H. Friedman and D. Chrzan, "Scaling theory of the Hall-Petch relation for multilayers," *Physical review letters,* vol. 81, pp. 2715, 1998.

[36] T. Suzuki, Y. Abe, M. Kawamura, K. Sasaki, T. Shouzu, and K. Kawamata, "Optical and electrical properties of pure Ag and Ag-based alloy thin films prepared by RF magnetron sputtering," *Vacuum,* vol. 66, pp. 501-504, 8/19/ 2002.

[37] Cox, N. D., et al., "Electrical Characterization of Carbon Nanotube Metal Matrix Composite Solar Cell Electrodes under Mechanical Stress," in *Photovoltaic Specialist Conference (PVSC), 2016 IEEE 43rd*, Portland, OR, pp. 1348-1350, 2016.

[38] Cox, N. D., et al., "Free-Standing Silver/Carbon Nanotube Metal Matrix Composite Thin Films," *Journal of Materials Science*, vol. 51, pp. 10935-10942, 2016.

LIST OF ACRONYMS, ABBREVIATIONS, AND SYMBOLS

Acronym/ Abbreviation	Description
AFRL	Air Force Research Laboratory
Ag	Silver
AM0	Air mass zero
CNT	Carbon nanotube
CVD	Chemical vapor deposition
Co	Cobalt
FSF	Free-standing film
HCl	Hydrochloric acid
HNO_3	Nitric acid
IMM	Inverted metamorphic multi-junction
InP	Indium phosphide
IPA	Isopropyl acohol
I-V	Current-voltage
MCE	Mixed cellulose ester
MMC	Metal matrix composite
MWCNT	Multi-walled carbon nanotube
NCTI	Nanocomp Technologies Inc.
Ni	Nickel
PCB	Printed circuit board
PVC	Polyvinylchloride
RACK	Resistance across cleaves and cracks
RIT	Rochester Institute of Technology
SDS	Sodium dodecyl sulfate
SEM	Scanning electron microscopy
SWCNT	Single wall carbon nanotube
TGA	Thermogravimetric analysis
Ti	Titanium
UTS	Ultimate tensile strength
UV	Ultraviolet
ZTJ	3rd generation triple junction

DISTRIBUTION LIST

DTIC/OCP
8725 John J. Kingman Rd, Suite 0944
Ft Belvoir, VA 22060-6218 1 cy

AFRL/RVIL
Kirtland AFB, NM 87117-5776 1 cy

Official Record Copy
AFRL/RVSV/David Wilt 1 cy